Coherent multi-meson photoproduction off a deuteron

Masterarbeit in Physik

von

Andreas Stirner

angefertigt im

Physikalischen Institut

vorgelegt der

Mathematisch-Naturwissenschaftlichen Fakultät
der Universität Bonn

September 2021

1. Gutachter: Prof. Dr. Hartmut Schmieden
2. Gutachter: Prof. Dr. Klaus Desch

Abstract

As a candidate for dark matter, the hexaquark d*(2380) comes into question. It can be found in various reaction channels. One of them is the coherent $2\pi^0$ photoproduction off a deuteron. As an extension to this, the coherent $3\pi^0$ photoproduction off a deuteron is investigated at the BGOOD experiment in Bonn and the differential cross-section for forward going deuterons ($\cos(\theta_{\mathrm{CMS}}) > 0.8$) is extracted for beam energies between 542 MeV and 2614 MeV. Furthermore, a look is taken into the invariant mass of $2\pi^0$d and π^0d. In addition, a method is developed to separate overlapping tracks of two photons in the BGO detector.

Table of contents

1 Note on notations

In the following thesis natural units are used with $c = \hbar = 1$. Accordingly, energies, momenta and masses have the same unit eV or multiples thereof. For four-momenta the abbreviation p without vector arrow is used and for three-momenta the abbreviation $\vec{p}$ with vector arrow. For the absolute value of a three-momentum, $|\vec{p}|$ is used. Furthermore, the first three components of four-momenta correspond to the components of the respective three-momenta, while the fourth component is the energy:

$$p = \begin{pmatrix} p_x \\ p_y \\ p_z \\ E \end{pmatrix}$$

2 Introduction

The existence of exotic hadrons was predicted by Freeman Dyson and Nguyen-Huu Xuong in 1964 and numerous research groups have conducted research in this field. In 2011, the WASA detector at the COSY accelerator in Jülich succeeded for the first time in identifying a hexaquark candidate. The discovery was confirmed in 2014 [1] [2]. It is the dibaryon d*(2380) which was found in the neutron-proton scattering via the nucleon fusion channels pn $\rightarrow \pi^0\pi^0$d and pn $\rightarrow \pi^+\pi^-$d. As a boson it is considered to be a candidate for a dark matter particle, since it is suspected that d*(2380) could form large stable Bose-Einstein condensates in the early phase of the universe [3].

Further experiments regarding new dibaryon resonances took place with the FOREST detector at ELPH in Sendai, Japan, in the photoproduction of $2\pi^0$ off a deuteron [4]. There, dibaryon candidates could be found that have a good match with the dibaryons predicted by Dyson and Xuong.

As an extension to the $2\pi^0$ photoproduction, the coherent photoproduction of $3\pi^0$ off a deuteron is investigated in this thesis at the BGOOD experiment at ELSA in Bonn. The differential cross-section for forward going deuterons with $\cos(\theta_{\mathrm{CMS}}) > 0.8$ is extracted for beam energies between 542 MeV and 2614 MeV and compared to the differential cross-section of $2\pi^0$ photoproduction. In addition, a look into the invariant mass distributions of $2\pi^0$d and π^0d is taken in the beam energy range between 939 MeV and 1303 MeV.

The structure of the thesis is as follows: Chapter 3 introduces the research context of this thesis from the 1960s until recent times, with focus on the study of dibaryons. Chapter 4 then gives an overview of the experimental setup of ELSA and the BGOOD experiment. Chapter 5 describes the event selection and event reconstruction. The further analysis steps to determine the differential cross section are then explained in chapter 6 and the results are discussed in chapter 7. Finally, the results are summarised again in chapter 8.

3 Research context

3.1 Multiplets of mesons and baryons (Gell-Mann, 1961)

After a large amount of strongly interacting particles, termed hadrons, had been discovered by the early 1960s, there were efforts to classify them. In 1961, Murray Gell-Mann created multiplets in which they were categorised [5]. The categorisation is based on different quantum numbers. One of them is the angular momentum J. This is integer for bosonic hadrons, the mesons, and half-integer for fermionic hadrons, the baryons. Another quantum number is parity P. It describes how a particle behaves upon reflection in space. Gell-Mann grouped baryons and mesons with the same combination of J and P into multiplets based on SU(3) symmetry. For the pseudoscalar mesons with $J^P = 0^-$, this results in an octet shown in Figure 1 (left), and also for the baryons with $J^P = \frac{1}{2}^+$ (right).

They are both sorted by strangeness S and charge Q. The meson octet contains the strange kaons with $S = \pm 1$ and the non-strange mesons, namely the pions and the η meson. In the middle at $S = 0$ and $Q = 0$, there are two particles in the same place that differ in isospin, the π^0 with $I = 1$ and the η with $I = 0$. Like the mesons, the baryons are sorted in the same pattern. For $S = 0$, there are the uncharged neutron and the positively charged proton, for $S = 1$ the Σ mesons and the Λ meson, which differ in isospin, and for $S = 2$ the two Ξ.

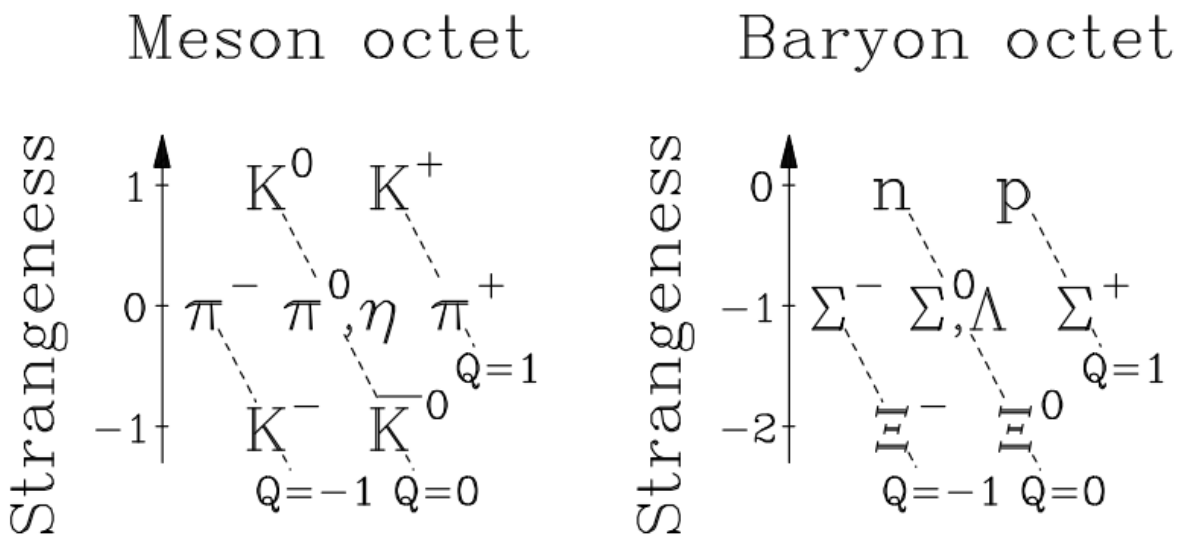

Figure 1: Multiplets of mesons with $J^P = 0^-$ (left) and baryons with $J^P = \frac{1}{2}^+$ (right) (taken from Ref. [6]).

3.2 Quark model (Gell-Mann, 1964)

To explain how his classification of mesons and baryons came about, Gell-Mann developed a model for the inner structure of hadrons in 1964 [7]. According to this model, hadrons are composed of elementary particles, which he called quarks. These come in three different flavours; up quarks (u), down quarks (d) and strange quarks (s). Gell-Mann assumed that quarks have a baryon number B of $\frac{1}{3}$ and that the baryon number of antiparticles is $-\frac{1}{3}$. Therefore, baryons (B = 1) consist of three quarks and mesons (B = 1) consist of one quark and one antiquark. Individual quarks do not occur, which today can be explained by the colour confinement.

3.3 Special mesons

In the following, two mesons are described in more detail that are particularly relevant for coherent $3\pi^0$ photoproduction.

3.3.1 Neutral pion

The neutral pion (π^0) is a pseudoscalar meson ($J^P = 0^-$) with the quark composition $(u\bar{u} - d\bar{d})/\sqrt{2}$ [8]. It has a mass of (134.9768 ± 0.0005) MeV and is thus the lightest of all mesons. It decays with a very short mean lifetime of $(8.43 \pm 0.13) \cdot 10^{-17}$ seconds, which makes it impossible to observe directly. Instead, the decay products can be observed. These are mostly two photons with a decay fraction of $(98.823 \pm 0.034)\%$. For example, with 3 pions, there is a probability of $(96.510 \pm 0.100)\%$ that they all decay into two photons each.

3.3.2 Eta meson

The eta meson (η) is a pseudoscalar meson ($J^P = 0^-$) with the quark composition of $(u\bar{u} + d\bar{d} - 2s\bar{s})/\sqrt{6}$ and a mass of 547.862 ± 0.017 MeV [8]. The η is of interest in the coherent $3\pi^0$ photoproduction, because it can create a background right due to two decay channels. On the one hand, it can decay into two photons with a probability of $(39.41 \pm 0.20)\%$, as does the π^0. On the other hand, it decays into $3\pi^0$ with a branching fraction of $(32.68 \pm 0.23)\%$.

3.4 Suggested multiplets of dibaryons (Dyson and Xuong, 1964)

After the deuteron, the nucleus of the hydrogen isotope ^{2}H, had long been the only known bound state with B = 2, Dyson and Xuong predicted other such states [9]. Unlike the deuteron, which consists of a proton and a neutron with 3 quarks each, the predicted dibaryons could possibly be single hadrons consisting of 6 quarks, so called hexaquarks. The predicted dibaryons form a sextet that is shown in Figure 2. They can be distinguished by isospin I and angular momentum J.

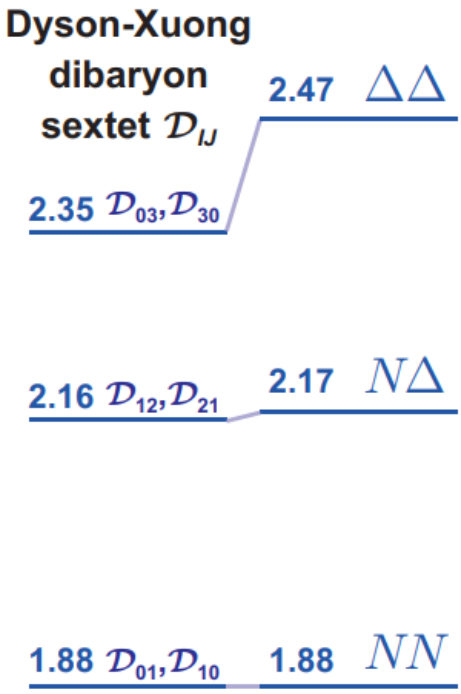

Figure 2: Dibaryons predicted by Dyson and Xuong forming a sextet. On the left is the dibaryon mass in GeV, on the right the sum of the corresponding baryon masses (taken from Ref. [4] and modified).

3.5 Recent research on dibaryons

3.5.1 d*(2380) at the COSY accelerator

In 2014, the first hexaquark candidate, d*(2380), was observed with the WASA detector at the COSY accelerator in Forschungszentrum Jülich [2]. It was produced in neutron-proton scattering and observed via the decay channels pn $\rightarrow \pi^0\pi^0$d and pn $\rightarrow \pi^+\pi^-$d. A resonance peak of an isoscalar dibaryon with $I(J^P) = 0(3^+)$ could be identified in the total cross-section that is shown in Figure 3. It has a mass of approximately 2380 MeV and a decay width of around 70 MeV. It could be associated with the $\Delta\Delta$ resonance predicted by Dyson.

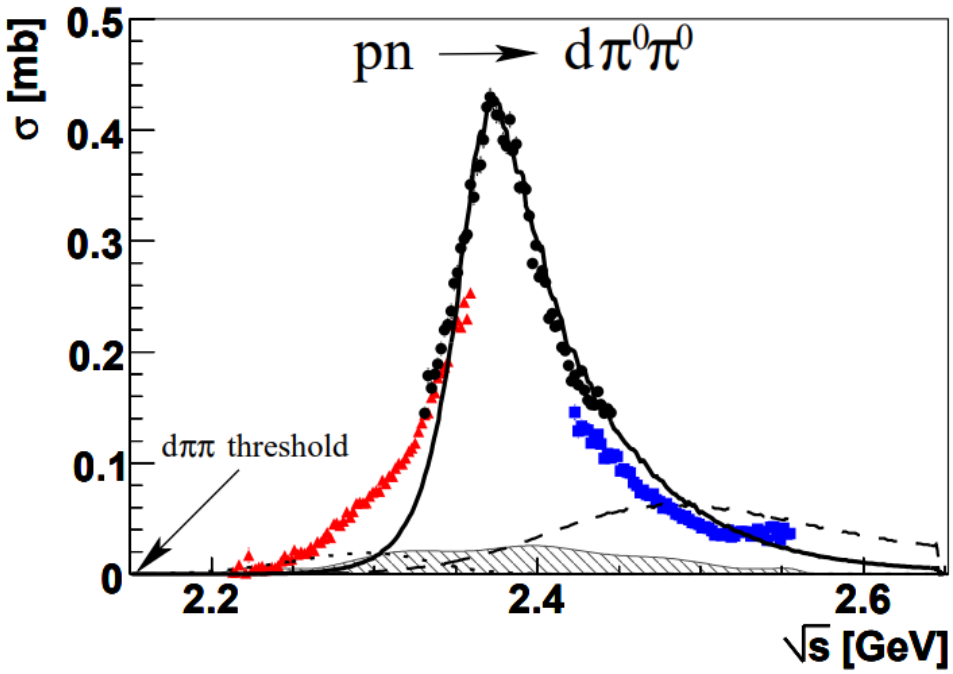

Figure 3: Total cross-section of pn $\rightarrow \pi^0\pi^0$d at COSY. A resonance was found at 2380 MeV (taken from Ref. [10]).

3.5.2 Coherent $2\pi^0$ photoproduction at ELPH

After the d*(2380) experiments in Jülich, research was carried out on other dibaryons, for example with the FOREST detector at the Research Center for Electron Photon Science (ELPH) in Sendai, Japan [11] [12] [4]. There, the coherent $2\pi^0$ photoproduction off a deuteron was investigated. It was expected that an isoscalar dibaryon resonance R_{IS} can be produced in the fusion of the photon and the deuteron, as shown in Figure 4. This can then decay into an isovector dibaryon resonance R_{IV} by emitting a π^0. The R_{IV} in turn then can decay into a deuteron under emission of another π^0.

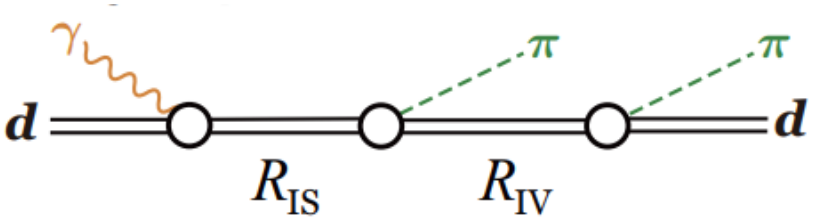

Figure 4: Example for a production of isoscalar and isovector dibaryon resonances in coherent $2\pi^0$ photoproduction off a deuteron (taken from Ref. [4]).

Isoscalar dibaryon resonances R_{IS} can be identified with the total cross-section in relation to the γd centre-of-mass energy, as shown in Figure 5. Two R_{IS} resonances with masses of 2.47 GeV and 2.63 GeV could be identified. A peak at 2.37 GeV can

also be seen which could possibly be the d*(2380). However, this one is not statistically significant.

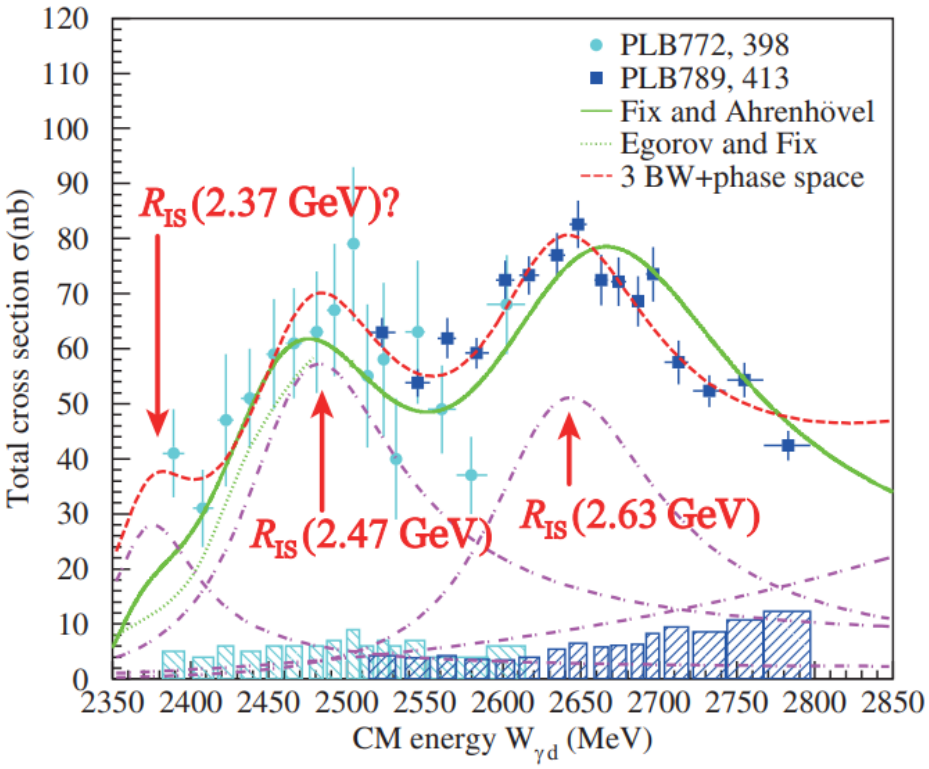

Figure 5: Total cross-section plotted against the centre-of-mass energy (taken from Ref. [4]).

In order to identify R_{IV} resonances, the invariant mass distribution of π^0d is shown in Figure 6. Here, a resonance-like structure is seen at 2.14 GeV.

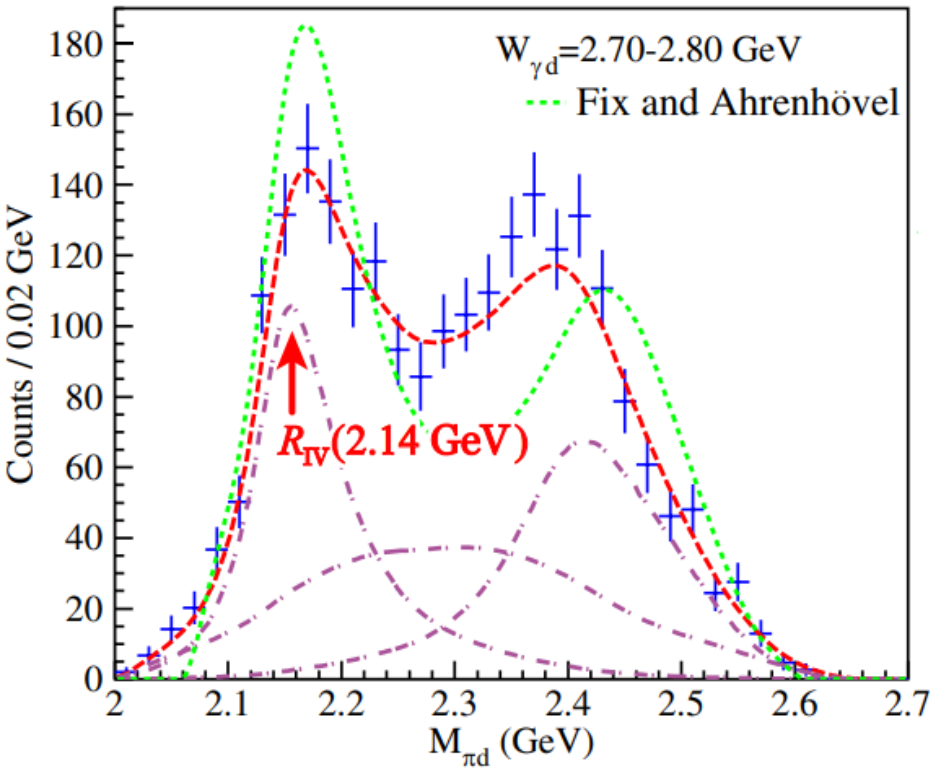

Figure 6: Distribution of the invariant mass of a π^0 and the deuteron (taken from Ref. [4]).

It turned out, that the dibaryons found with the FOREST detector have a good match with the dibaryons predicted by Dyson and Xuong [4].

3.5.3 Coherent $3\pi^0$ photoproduction at ELSA

Inspired by the coherent $2\pi^0$ photoproduction off a deuteron at ELPH where dibaryon resonances have been found, this is extended to coherent $3\pi^0$ photoproduction off a deuteron in this thesis. Based on the results from ELPH, one could expect, in this reaction channel, isovector resonances in the differential cross-section of $\gamma d \rightarrow 3\pi^0 d$ and the invariant mass of $\pi^0 d$ as well as isoscalar resonances in the invariant mass of $2\pi^0 d$. This is investigated at the BGOOD experiment at ELSA in Bonn, whose experimental setup is described in more detail in the following chapter.

4 Experimental setup and data collection

4.1 Electron stretcher facility

The electron stretcher facility, or ELSA for short (for "Elektronen-Stretcher-Anlage" in German), is a particle accelerator that delivers electrons with energies of up to 3.2 GeV [13]. These can be used for various experiments in hadron physics such as CB-ELSA or BGOOD. The setup of ELSA is shown in Figure 7. First, an electron source provides electrons with 50 keV, which are accelerated to 26 MeV in the linear accelerator LINAC. Then they are fed into the circular booster synchrotron with a diameter of 70 metres and accelerated up to 1.6 GeV. After this, they reach their final energy of 3.2 GeV in the 164 metre circumferential stretcher ring, from where they can be fed into the two experiments.

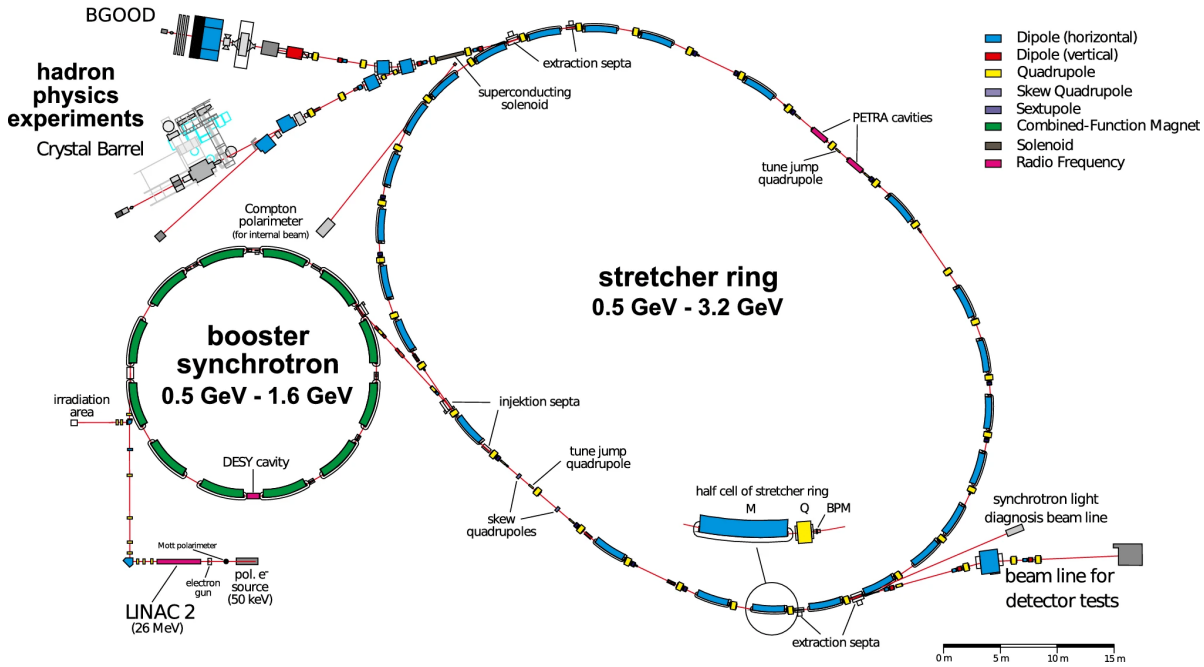

Figure 7: Experimental setup of ELSA (originated from Ref. [14], modified in Ref. [13]).

4.2 The BGOOD experiment

The BGOOD experiment shown in Figure 8 is one of the two hadron physics experiments at the ELSA facility [13]. It is well suited for the investigation of hadron resonances and meson photoproduction. Electrons from ELSA are used to produce high-energy photons via bremsstrahlung, which hit a fixed target. Surrounding the target is the rugby ball shaped BGO calorimeter for the detection of neutral and charged particles in a solid angle range of $0.9 \cdot 4\pi$. There is also a magnetic spectrometer with an open dipole (OD) magnet for the identification of forward-going particles. A more detailed overview of the setup of the BGOOD experiment can be found in Ref. [13]. The following sub-

subchapters cover those components that are particularly relevant for coherent multi-meson photoproduction.

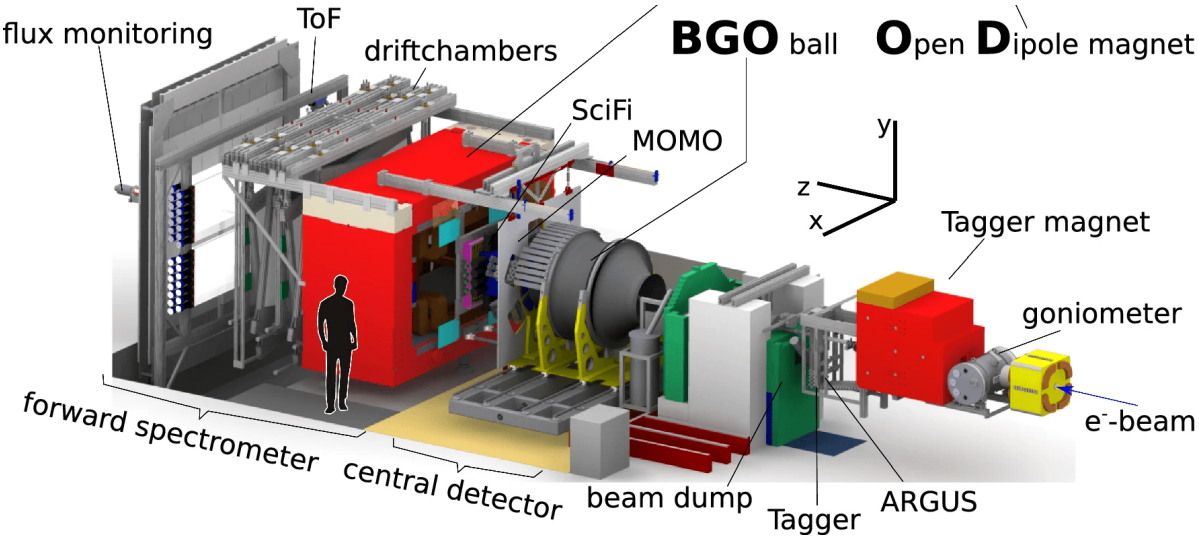

Figure 8: Experimental setup of the BGOOD experiment (taken from Ref. [13]).

4.2.1 Tagging system

The unpolarised electron beam from ELSA with an energy of 3.2 GeV first hits the diamond radiator, where photons in the range of 320 MeV to 2880 MeV are generated via bremsstrahlung. The energy of the photons is then determined via the remaining energy of the electrons. For this purpose, the electrons are deflected with a magnetic dipole. The energy can then be determined from the angle of deflection. The energy of the tagger photon then follows from the difference between the initial and the final energy of the electron.

4.2.2 Target

The photon hits a fixed target inside the BGO ball. Either liquid hydrogen (protium or deuterium) targets or solid targets such as carbon are used. In this case, liquid deuterium is applied, which is located in an 11 cm long target cell made of aluminium.

4.2.3 BGO rugby ball calorimeter

The BGO calorimeter shown in Figure 9 is an electromagnetic calorimeter consisting of 480 bismuth germanium oxide ($Bi_4(GeO_4)_3$) crystals. These scintillation crystals are arranged cylindrically symmetrically around the beam axis with 32 crystals in the azimuthal direction times 15 crystals in the polar direction. In this way, the BGO calorimeter can cover a polar angular (θ) range from 25° to 155° as well as the complete azimuthal angular (ϕ) range. This results in a solid angle of $0.9 \cdot 4\pi$.

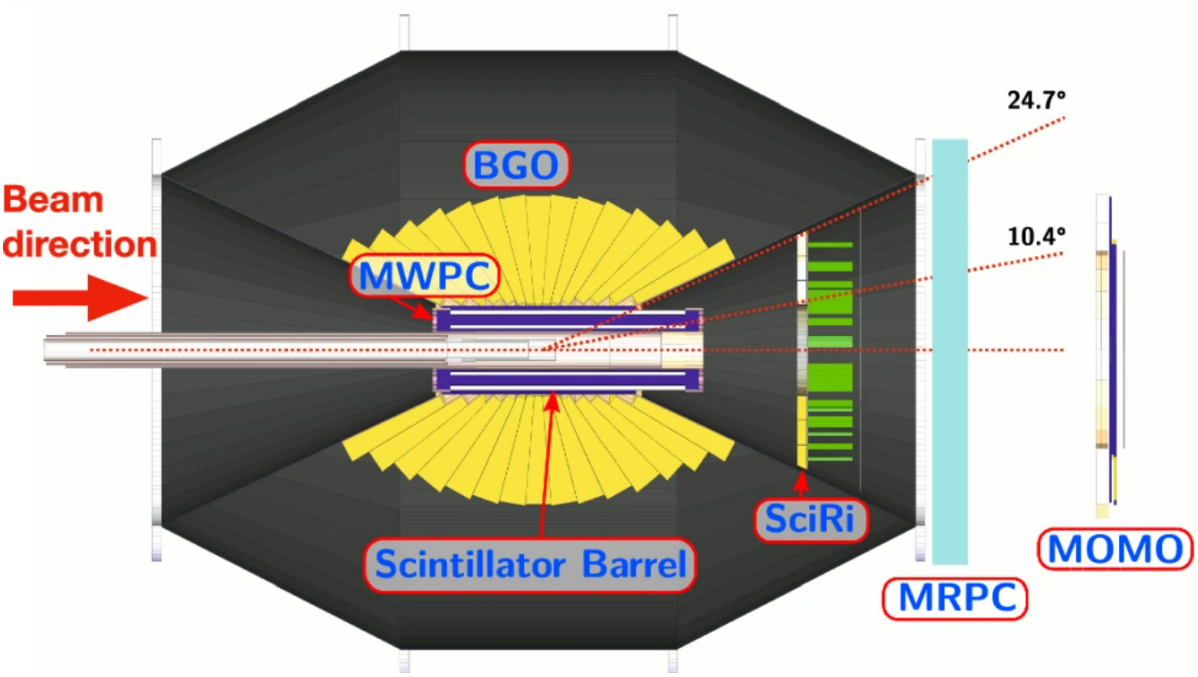

Figure 9: Experimental setup of the BGO ball (taken from Ref. [13]).

The individual crystals have an angular expansion of 11.25° in azimuthal direction and in average 8.67° in polar direction. However, because tracks from photons and electrons form clusters in several neighbouring crystals, the direction of such a track can be measured with a higher resolution than the crystal expansion. For this purpose, the mean of the distribution of the deposited energy in these neighbouring crystals can be determined. The deposited energy of each crystal, in turn, is measured with photomultipliers behind the crystals with a resolution of 3% for 1 GeV photons. Between the target and the BGO ball are plastic scintillators to distinguish uncharged particles such as photons from charged particles and multiwire proportional chambers to track charged particles. The BGO detector is thus well suited for the reconstruction of mesons that decay into photons, such as π^0 and η, by determining the invariant mass of such photons.

4.2.4 Forward spectrometer

The forward spectrometer consists of an open dipole magnet through which charged particles are directed onto a curved track. In front of and behind the magnet are detectors to determine the trajectory and thus the momentum of the particles with an angle resolution of 1° and a momentum resolution of 3%. In front there are the scintillating fibre detectors MOMO and SciFi, and behind there are eight double-layer drift chambers. Behind the drift chambers is the time-of-flight-detector (TOF) for determining the velocity β. With the momentum and the velocity β of the particles, the mass of the particles can thus be determined. The mass is noticeable as a curve in a plot of

momentum against β, as shown in Figure 10, where each yellow line corresponds to a different particle with a specific mass. For example, the lines from left to right correspond to pions, kaons and protons in this diagram. The forward spectrometer is thus well suited for the identification of the forward-going deuterons, which makes it possible to distinguish coherent from incoherent events.

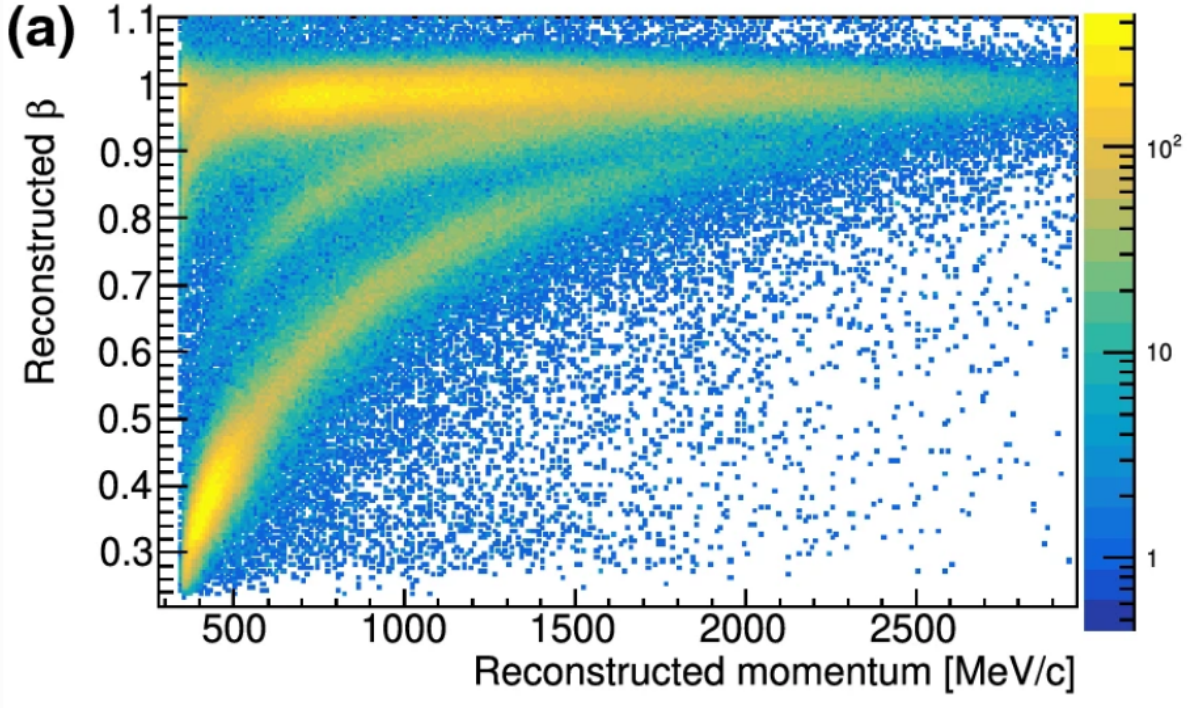

Figure 10: Momentum in forward spectrometer plotted against β. In this example a proton target is used. The yellow lines from left to right correspond to pions, kaons and protons (taken from Ref. [13]).

4.3 Data collection

In the thesis, the ELSA beam time from 13th June 2018 to 9th July 2018 with the run numbers from 41469 to 45872 is considered. Only the runs with a full liquid deuterium target are selected. A total of around $3.12 \cdot 10^9$ events were recorded in 3397 runs. In addition to the real data, 100 million events are simulated with Monte Carlo simulation for each individual reaction channel. This is the main channel $\gamma d \to 3\pi^0 d$, the channel $\gamma d \to 2\pi^0 d$ for comparison and the channel $\gamma d \to \eta d$, since an η resonance is expected in the invariant mass of $3\pi^0$. In the main channel, 9.8 million events were lost because the first runs crashed, so there are only 90.2 million events in total. Furthermore, only 50 million simulated events are considered in the figures in the next chapter 5. However, the further analysis from chapter 6 are based on all simulated events. The simulated events are later used to calculate the detection efficiency and to remove background from the signal.

5 Event selection and event reconstruction

Due to the high number of recorded events, of which only a small fraction is of interest for this topic, the number of events is reduced by several selection criteria. In addition, the π^0 are reconstructed in the selected events with the help of the photon tracks in the BGO, since the π^0 cannot be measured directly due to their short lifetime. For this event selection and event reconstruction, the software Explora is used.

5.1 Initial State

5.1.1 Tagger photon

Since a photon hits a deuteron in the initial state, only those events are selected that contain exactly one track in the tagger. After this first cut, about $2.95 \cdot 10^9$ of the original $3.12 \cdot 10^9$ events remain, which corresponds to 94.3 %. In about 2.6 % of all events, no track is reconstructed in the tagger and in the remaining 3.1 %, there are at least two tracks in the tagger. After the cut, the beam energy E_{Beam} of the photon is determined for every single event. This is shown in Figure 11. The distribution of the number of events per tagger channel fits well with the expected bremsstrahlung cross-section, which depends on the inverse photon energy $1/E_{Beam}$ [15].

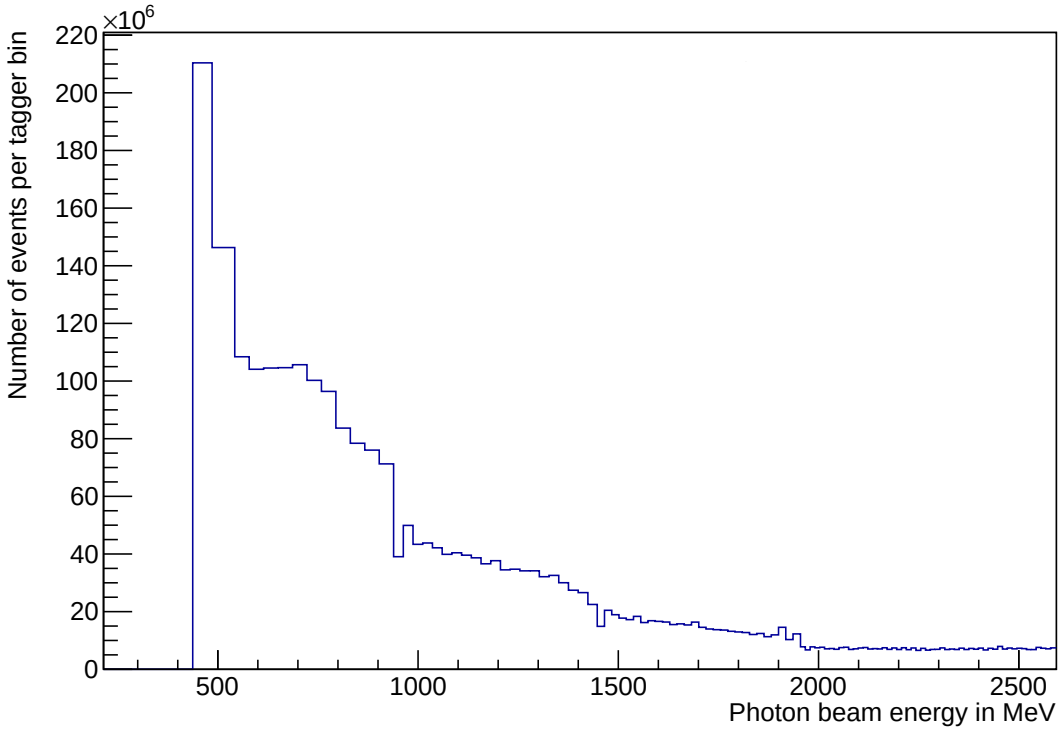

Figure 11: Distribution of the beam energy.

The next step is to determine the four-momentum p_{Beam} of the tagger photon. It is assumed that the photon propagates in z-direction. Thus, the four-momentum is calculated as:

$$p_{Beam} = \begin{pmatrix} 0 \\ 0 \\ E_{Beam} \\ E_{Beam} \end{pmatrix}$$

5.1.2 Deuteron target and centre-of-mass-system

It is known from thermodynamics that the mean kinetic energy of a particle as a dependency of the temperature is of the order of $k_B T$, with the Boltzmann constant $k_B = 8.6 \cdot 10^{-5} JK^{-1}$ [16] and the temperature T, which is below the boiling temperature of deuterium. Since this is many orders of magnitude below the energies of the tagger photons, one can neglect the initial kinetic energy of the deuteron in comparison. Accordingly, a static target with no three-momentum and $E_{Target} = m_{Target}$ is assumed. The four-momentum p_{Target} is thus:

$$p_{Target} = \begin{pmatrix} 0 \\ 0 \\ 0 \\ m_{Target} \end{pmatrix}$$

The four-momentum p_{cms} of the total system is then the sum of the four-momenta of the tagger photon and the deuteron target:

$$p_{cms} = p_{Beam} + p_{Target} = \begin{pmatrix} 0 \\ 0 \\ E_{Beam} \\ E_{Beam} + m_{Target} \end{pmatrix} \tag{1}$$

5.2 Final State

In the event selection for the final state, the general case of a photoproduction of $n_\pi \in \mathbb{N}$ neutral pions (π^0) is considered first, with n_π being specified later. Initially, both coherent and incoherent events are selected, as the incoherent events are later used to determine the background, among other things.

5.2.1 Preselection

In the final state, there is a deuteron in the coherent events or a proton in the incoherent events as well as the $n_\pi \pi^0$, each of which decays into two photons, making $2n_\pi$ photons in total. The aim is now to select events in which the proton or deuteron enters the forward spectrometer and the photons enter the BGO. Therefore, events that have tracks in the intermediate SciRi detector or charged tracks in the BGO are cut away. In addition, an

event must have exactly one charged track in the forward spectrometer. For the number of uncharged tracks in the BGO, a cut is applied later, since the number of π^0 is not further specified yet. After these cuts, $1.11 \cdot 10^7$ events remain, which is around 0.36% of the originally recorded events.

5.2.2 Particle in the forward spectrometer

To distinguish coherent from incoherent and other events, the mass of the particle in the forward spectrometer is determined. Figure 12 shows the distribution of the mass with real data (left) and simulated $\gamma d \to 3\pi^0 d$ data (right). In the left diagram for the real data, a peak around the proton mass with approximately $1.6 \cdot 10^5$ events per 5 MeV is clearly visible. Also clearly visible is a peak around the π^0 mass with around $1.0 \cdot 10^5$ events per 5 MeV. There is also a small peak around the kaon mass. The deuteron peak, on the other hand, is very difficult to see on the diagram. In the right diagram for the simulated data, a peak around the deuteron mass can be seen, as expected, but also a little peak around the proton mass.

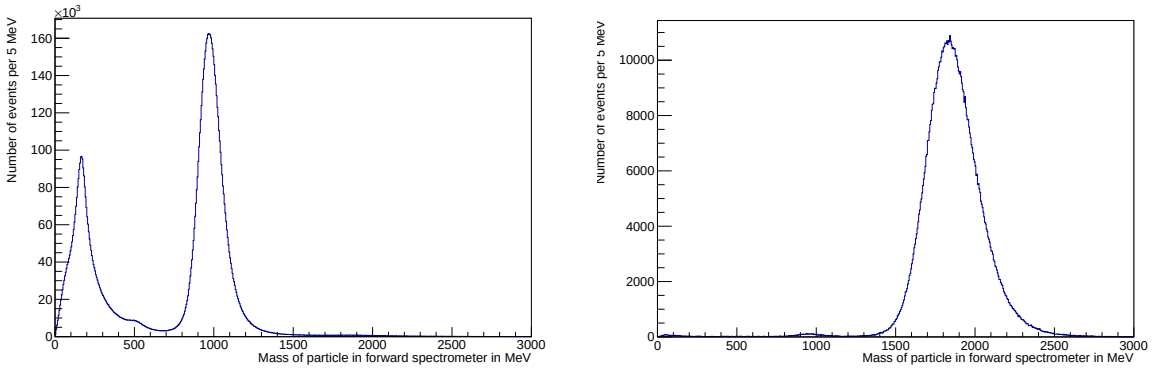

(a) Real data

(b) Simulated $\gamma d \to 3\pi^0 d$ data

Figure 12: Distribution of the mass in the forward spectrometer with a linear scale.

To make the deuteron peak in the left diagram visible, Figure 13 shows the mass distribution with a logarithmic scale, while Figure 14 shows it on a linear scale, but zoomed in on the deuteron peak.

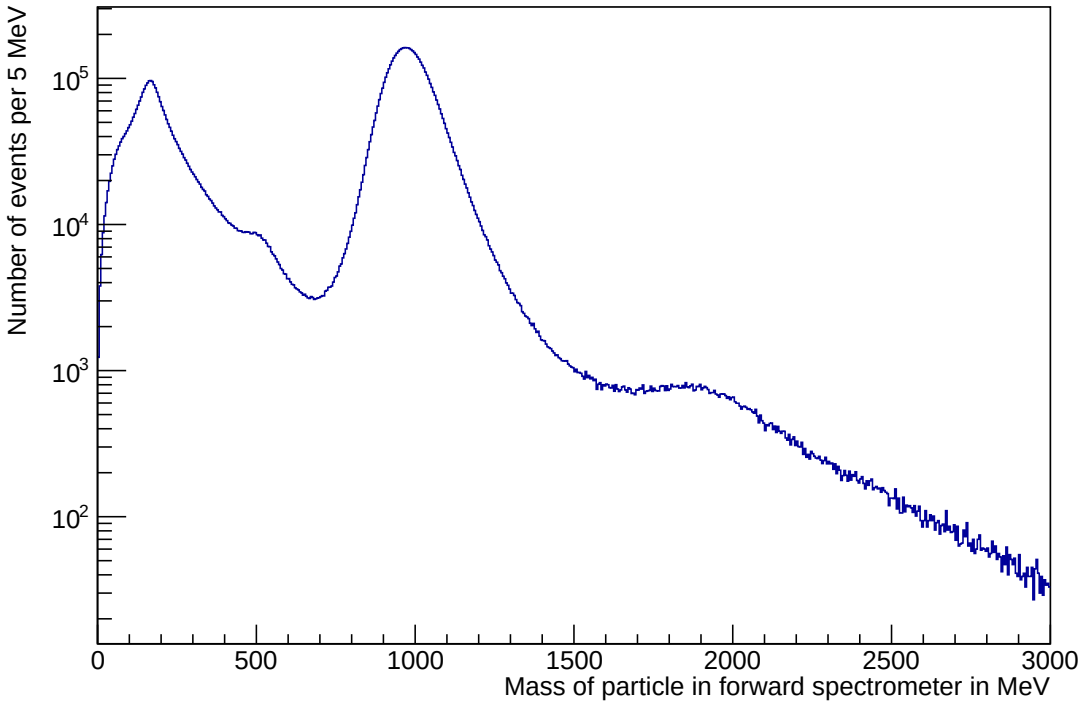

Figure 13: Distribution of the mass in the forward spectrometer with a logarithmic scale (real data).

Now the events are sorted into two groups. Those with a mass between 800 and 1200 are initially assumed to be incoherent events, those with a mass between 1600 and 2400 as coherent events. All other events are cut away. However, as can be seen in Figure 14, there is a non-negligible incoherent background in the events that are initially classified as coherent. In total, 87265 events classified as coherent and around $5.9 \cdot 10^6$ events classified as incoherent are left in the real data after these cuts. The next step is to determine the four-momentum of the forward particle. For this purpose, the mass of the particle in the coherent events is set to the exact mass of the deuteron, while in the incoherent events it is equated with the exact proton mass.

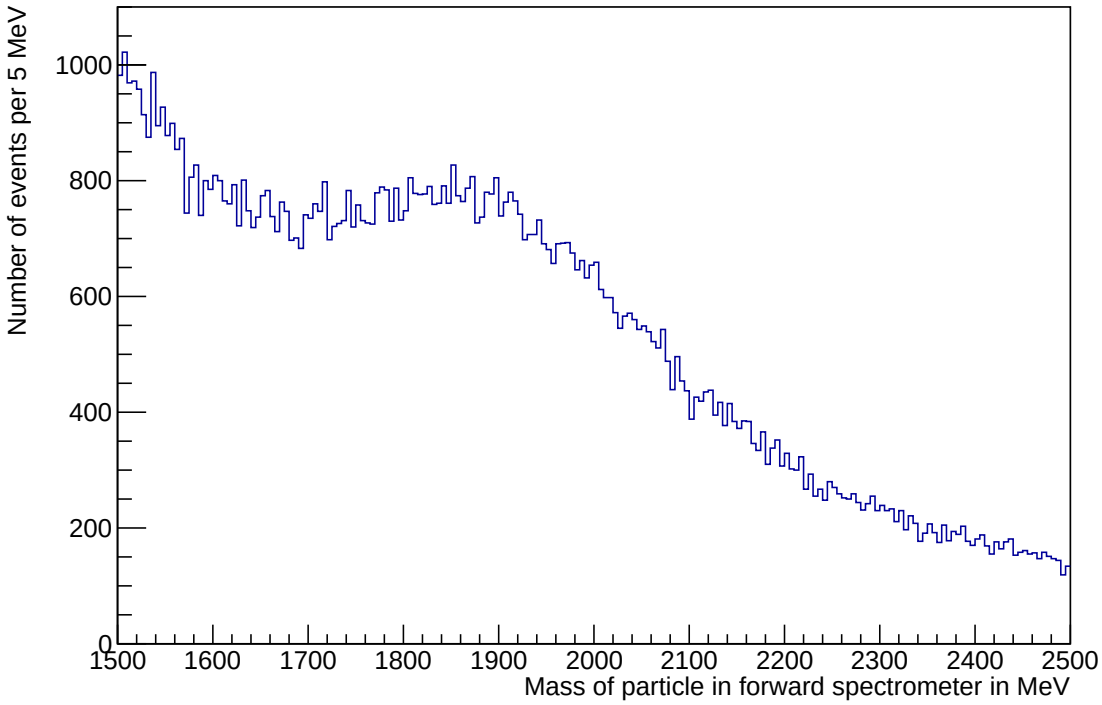

Figure 14: Distribution of the mass in the forward spectrometer with a linear scale, zoomed into the deuteron peak (real data).

5.2.3 Photons in the BGO

In order to reconstruct mesons like π^0 and η, it is first assumed that all uncharged tracks in the BGO ball are photons. Before the meson reconstruction, the energies $E_{\gamma i}$ and the two angles $\phi_{\gamma i}$ and $\theta_{\gamma i}$ are determined, where γi stands for the i-th photon. With the relation $E = |\vec{p}|$, the complete four-momentum $p_{\gamma i}$ can then be determined for each photon, which is later needed to calculate the invariant mass of several photons.

As an example, Figure 15 shows the energy distribution for single photons. They all have a minimum energy of over 25 MeV because of a threshold applied in the clustering. The peak of the distribution is between 50 and 100 MeV. This is also to be expected, for example, when a π^0 at rest decays, since the photons in the pion's rest system must have exactly half the mass of the π^0 due to conservation of momentum and energy. However, much higher energies still occur due to a kinetic energy of the π^0 and due to photons that do not originate from π^0 decay, as can be seen in the figure.

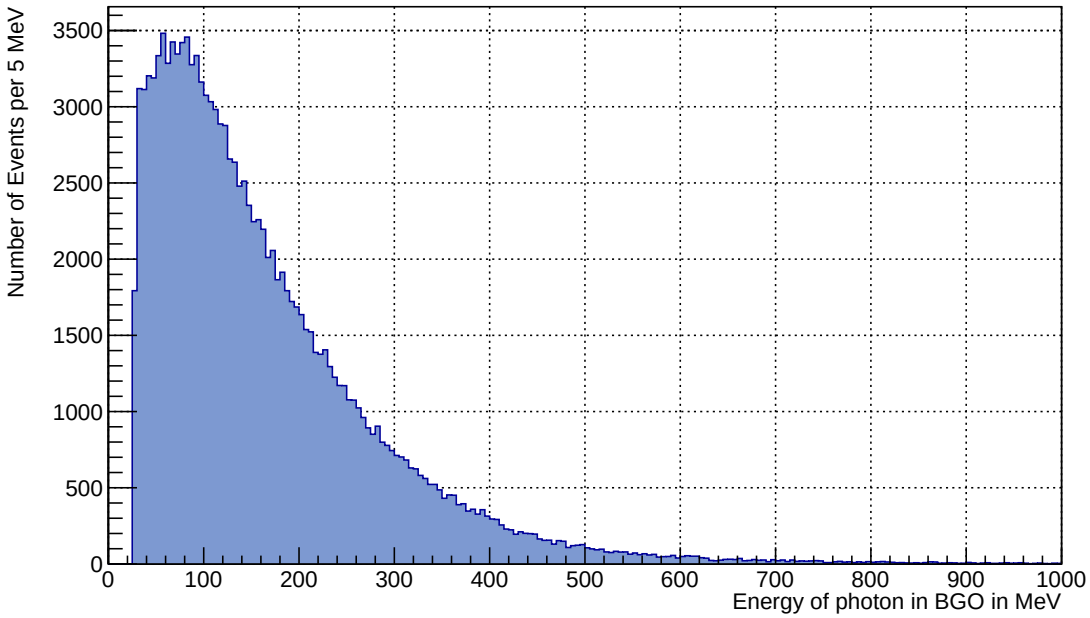

Figure 15: Energy of each photon in the BGO

The events are then sorted according to the number of photons. As a candidate for an $\gamma d \rightarrow n_\pi \pi^0 d$ event, events with $2n_\pi$ photons are considered. Likewise, events with $2n_\pi - 1$ photons are classified as candidates for an event with n_π pions, where the tracks of two photons overlap. Later, such tracks will be separated into two individual tracks. For example, events with 5 or 6 photons are classified as potential $3\pi^0$ events.

5.2.4 Missing particles

Since the detector does not cover the entire solid angle of 4π and photons or other particles can thus fly past the detector or are not detected for other reasons, the events are cut away in which particles are presumably lost. To do this, the sum p_{sum} of all four-momenta of the photons in the BGO is formed:

$$p_{sum} = \sum_{i=1}^{n_\gamma} p_{\gamma i}$$

Subsequently, the missing four-momentum p_{miss} of all photons relative to the centre-of-mass four-momentum p_{cms} from equation 1 is determined:

$$p_{miss} = p_{cms} - p_{sum}$$

In the coherent events, the missing mass, i.e. the mass of the missing four-momentum $\sqrt{{p_{miss}}^2}$, should correspond to the deuteron mass, and the missing momentum should correspond to the momentum of the particle in the forward spectrometer. In addition,

the angle between the missing four-momentum and the particle in the forward spectrometer should be as small as possible. All cuts described in this sub-subchapter are only applied at the end of the sub-subchapter.

Figure 16 shows the distributions of the missing mass in real coherent and simulated coherent events with 6 and 5 uncharged tracks in the BGO. For 6 tracks, a sharp peak is seen around the deuteron mass in both real and simulated data, which is to be expected for coherent $3\pi^0$ events. In comparison, in the diagram for 5 tracks the distribution is slightly shifted to the right, which is probably mainly due to $\gamma d \rightarrow 3\pi^0 d$ events where a photon has been lost, making the missing mass larger than the deuteron mass. However, even here there are many events where the missing mass is approximately equal to the deuteron mass. This is expected, for example, when two photons overlap into a single track in $\gamma d \rightarrow 3\pi^0 d$ events. In both real distributions with 6 and 5 uncharged tracks in the BGO, a broadening to the right is also visible. This can come from an incoherent background as well as from a background of other reaction channels where even more photons have been produced.

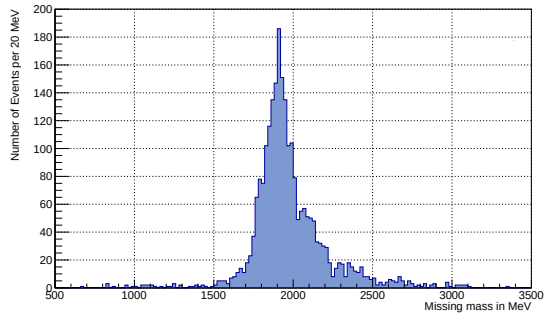

(a) Real events with $n_\gamma = 6$

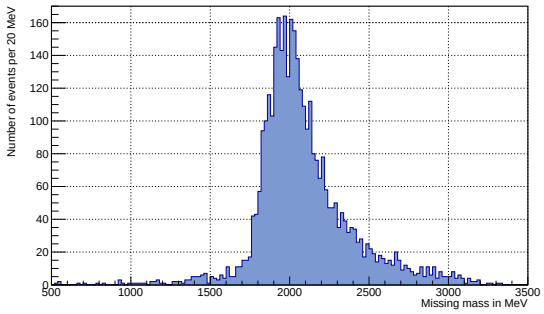

(b) Real events with $n_\gamma = 5$

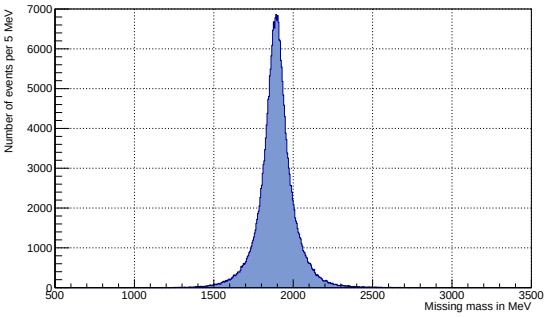

(c) Simulated events with $n_\gamma = 6$

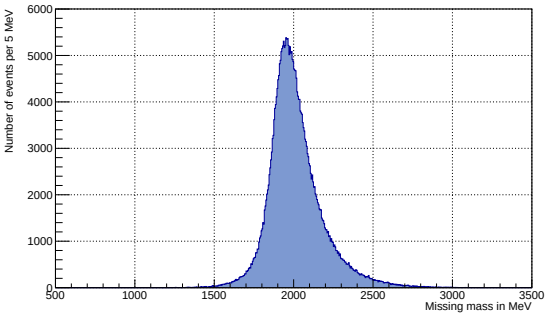

(d) Simulated events with $n_\gamma = 5$

Figure 16: Distribution of the missing mass of all photons in the BGO in relation to the centre-of-mass four-momentum p_{cms} in coherent events.

For comparison, Figure 17 shows the distributions of the missing mass of real coherent events and simulated coherent $2\pi^0$ events with 4 and 3 photons. In the simulated data

with 4 tracks, a clear peak is found at the deuteron mass, which is to be expected in the decay of $2\pi^0$. With 3 tracks, the distribution is broadened to the right, which indicates lost photons. However, here too the peak is at the deuteron mass, presumably due to overlapping of two photons into a track. The distributions of the real events are both spread further to the right, since events other than $2\pi^0$ events as well as the incoherent background can also play a role here.

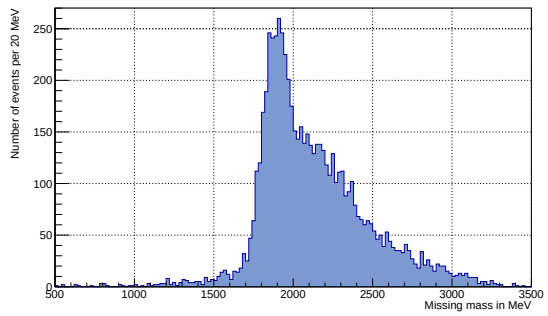

(a) Real events with $n_\gamma = 4$

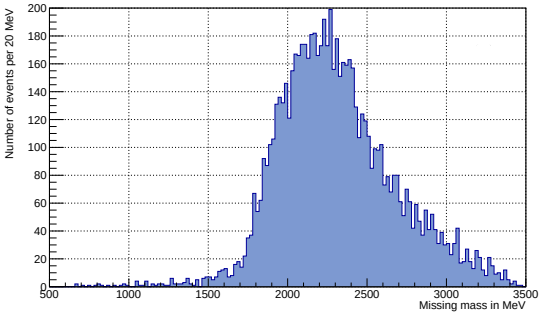

(b) Real events with $n_\gamma = 3$

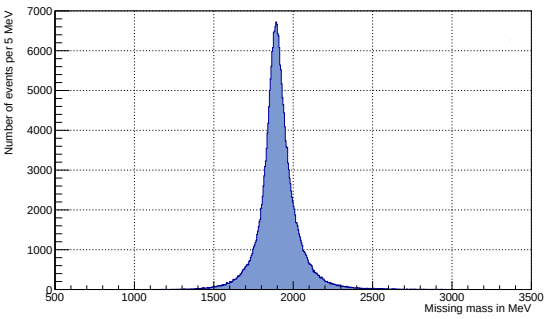

(c) Simulated events with $n_\gamma = 4$

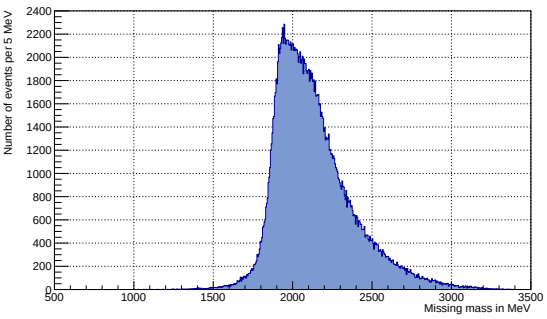

(d) Simulated events with $n_\gamma = 3$

Figure 17: Distribution of the missing mass of all photons in the BGO in relation to the centre-of-mass four-momentum p_{cms} in coherent events.

Figure 18 shows the distributions of the missing mass in real incoherent events with 6 and 4 uncharged tracks, where a proton is selected in the forward spectrometer. These also show a broadening on the right side. However, this can also be due to a momentum between the proton and the neutron, meaning that the invariant mass of the proton and the neutron is higher than the deuteron mass and thus the missing mass of the photons which should be equal to the invariant mass of proton and neutron.

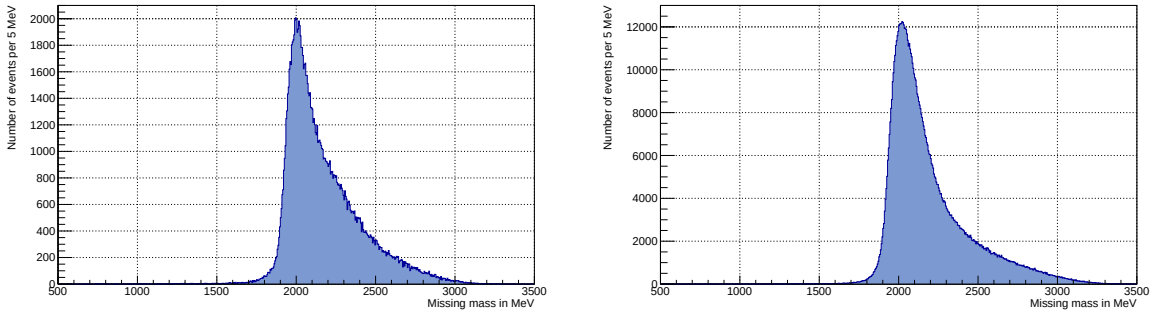

(a) Events with $n_\gamma = 6$

(b) Events with $n_\gamma = 4$

Figure 18: Distribution of the missing mass of all photons in the BGO in relation to the centre-of-mass four-momentum p_{cms} in real incoherent events.

To reduce the background of events with missing particles, a cut is applied to coherent events and all events are cut away where the missing mass differs from the deuteron mass by more than 250 MeV. For incoherent events, the missing mass must not deviate from the deuteron mass by more than 250 MeV in the downward direction only. However, it may be significantly larger, since the invariant mass of proton and neutron can be larger than the deuteron mass due to a possible momentum between proton and neutron. Thus, no cut upwards is applied to incoherent events with a selected proton in the forward spectrometer.

Figure 19 shows the missing momentum of all photons compared to the momentum of the forward particle for real coherent (left) and simulated coherent $3\pi^0$ (right) events. As expected, most events lie along a diagonal line where both momenta are equal. In addition, there are some events where the missing momentum is significantly larger than the momentum of the forward particle. These events are cut away later because photons were probably lost here. In the real data, there are also events with a forward momentum significantly higher than the missing momentum, especially in a region around 2000 MeV for the forward momentum and 500 MeV for the missing momentum. At a distance of 500 MeV from the diagonal, a cut is applied to the coherent events on both sides.

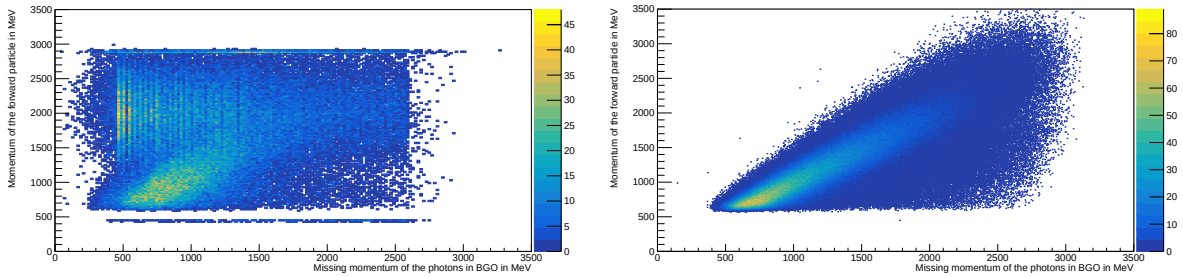

(a) Real data. 20 MeV per bin.

(b) Simulated $\gamma d \to 3\pi^0 d$ data. 5 MeV per bin

Figure 19: Missing momentum of all photons in the BGO versus momentum of the deuteron in the forward spectrometer (coherent data).

Figure 20 now shows the missing momentum of all photons compared to the forward momentum in real incoherent events with a proton in the forward spectrometer. Again, many events lie around the diagonal. Due to a momentum between proton and neutron, there are also, as expected, events where the missing momentum is larger than the forward momentum. Since this is not due to missing particles, the cut of 500 MeV described above is only applied above the diagonal for incoherent events.

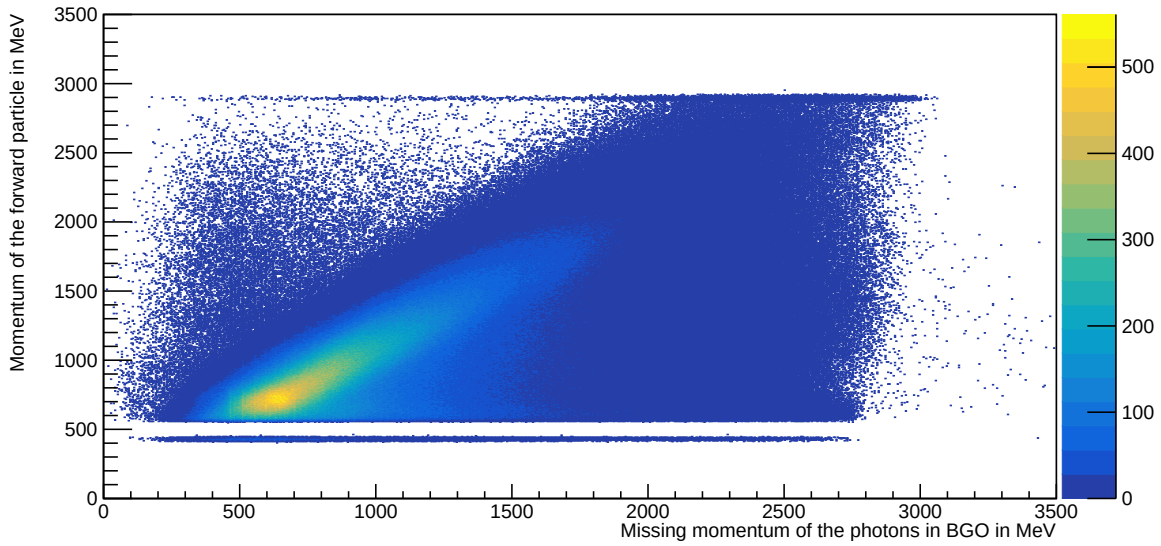

Figure 20: Missing momentum of all photons in the BGO versus momentum of the deuteron in the forward spectrometer (real incoherent data).

Finally, the angle between the missing momentum of the photons and the momentum of the particle in the forward spectrometer is considered, shown in Figure 21. On the left is real coherent data, on the right simulated coherent $3\pi^0$ data. Events with an angle greater than 10° are cut away.

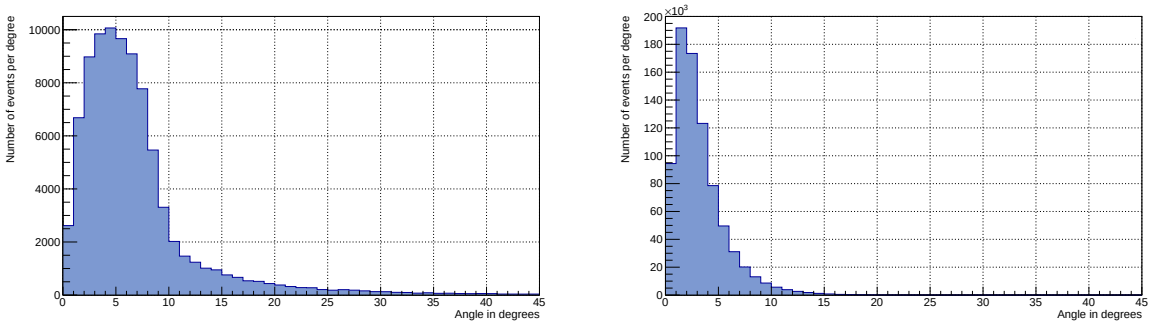

(a) Real coherent data

(b) Simulated $\gamma d \rightarrow 3\pi^0 d$ data

Figure 21: Difference in angle between the missing momentum of the photons and the the momentum of the forward deuteron.

5.2.5 Reconstruction of π^0

To reconstruct the neutral pions in events with an even number $2n_\pi$ of photons, all photons are first sorted into pairs. All possible combinations are tried out once, for example a total of 15 combinations of 6 photons. For each pair, the invariant mass is determined, which can be seen in Figure 22, where a clear peak around the π^0 mass is visible. In order for a combination to be classified as a potential candidate for a $n_\pi\pi^0$ photoproduction, all invariant masses of the pairs must approximately correspond to the π^0 mass. The cut for the difference is set to 35 MeV based on Figure 22. If there are several potential candidates for such an event, the combination is selected for which the sum of the squared differences between the invariant mass to the π^0 mass is smallest.

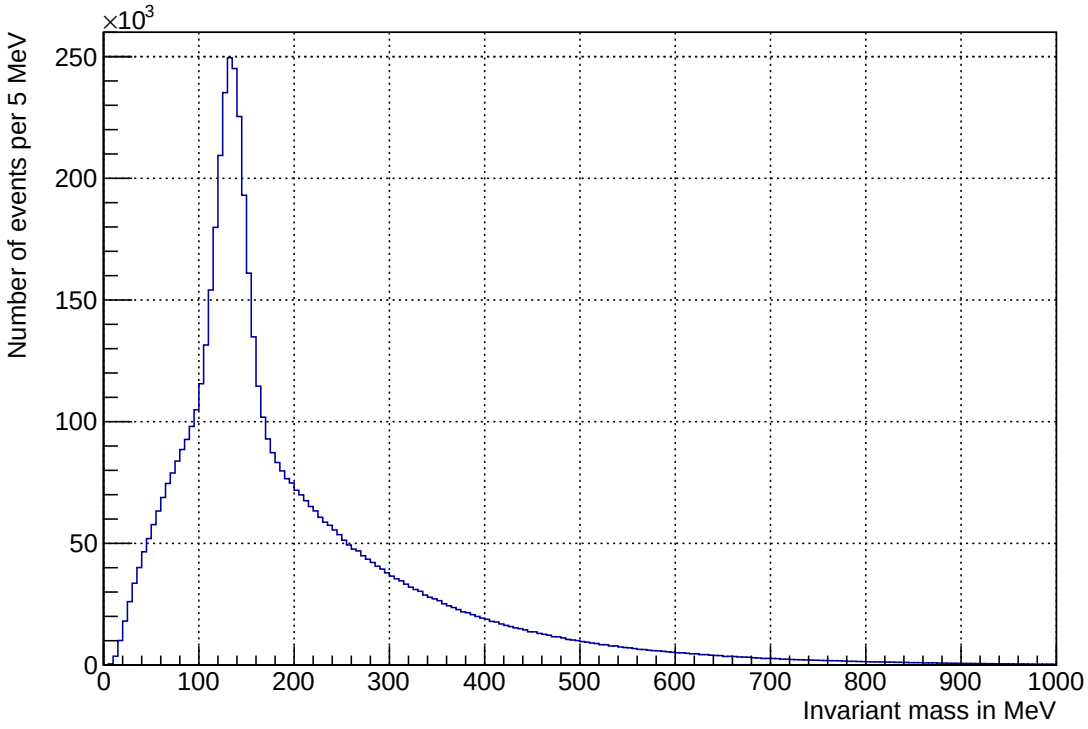

Figure 22: Invariant mass of each possible pair of photons.

5.2.6 Overlapping photon tracks

It is possible for the tracks of two photons to overlap into a single track. In this case, there are $2n_\pi - 1$ uncharged tracks in the BGO, provided that no other photon is lost. To increase the efficiency, such tracks where two photons overlap are tried to separate into the two original tracks. The prerequisite for this method is that both photons come from two different π^0.

First, two pions π_A and π_B are assumed that decay into the following photons:

$$\pi_A \to \gamma_{A1} + \gamma_{A2} \qquad \text{and} \qquad \pi_B \to \gamma_{B1} + \gamma_{B2}$$

This is also shown in Figure 23. Next, it is assumed that γ_{A2} and γ_{B2} overlap into a track, which is initially misinterpreted as a single photon γ_2. Now, to reconstruct the four-momenta of γ_{A2} and γ_{B2}, the flight direction of γ_{A2} and γ_{B2} is set equal to the direction of γ_2. It follows from this:

$$\phi_{A2} = \phi_{B2} = \phi_2 \qquad \text{and} \qquad \theta_{A2} = \theta_{B2} = \theta_2$$

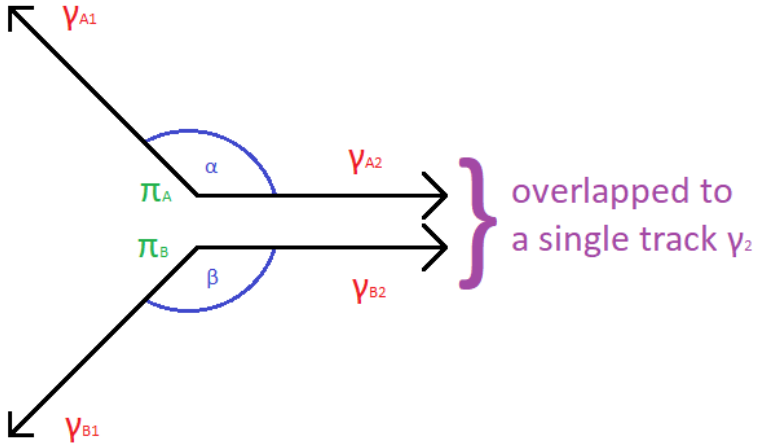

Figure 23: Sketch of two overlapping photon tracks.

With known directions, the angle α between γ_{A1} and γ_{A2} and the angle β between γ_{B1} and γ_{B2} can then be determined. To determine the energy of γ_{A2} and γ_{B2}, one can make use of the fact that the invariant mass of the two photons of the same π^0 must correspond to the π^0 mass m_π and that the energy of a photon corresponds to its momentum. This means that:

$$m_\pi^2 = (p_{A1} + p_{A2})^2 = 2E_{A1}E_{A2} - 2\vec{p}_{A1} \cdot \vec{p}_{A2} = 2E_{A1}E_{A2}(1 - \cos(\alpha))$$

By conversion one then obtains the energy of γ_{A2}:

$$E_{A2} = \frac{m_\pi^2}{2E_{A1}(1 - \cos(\alpha))}$$

E_{B2} is calculated analogously. To ensure that the above assumptions are likely to be met, the condition that the sum of the energies of the original tracks E_{A2} and E_{B2} is approximately equal to energy E_2 of the total overlap tracks must be fulfilled.

In practice, with 3 uncharged tracks in the BGO, each track in turn is assumed to be an overlap of two photons and this condition is checked. Figure 24 shows the difference $(E_{A2} + E_{B2}) - E_2$ accordingly. The condition is considered fulfilled if the difference is smaller than a cut of 30 MeV. The overlap track is then separated into two tracks. The total energy is split between the two tracks proportionally to E_{A2} and E_{B2} so that the total energy remains constant. The direction is also maintained and corresponds to the direction of the old track for both new tracks. If there are 5 uncharged tracks, it is first proceeded as in the previous sub-subchapter. If exactly one π^0 can be reconstructed, the remaining three uncharged tracks are searched for overlaps. If they can be separated into four tracks in this step, another attempt is made to reconstruct another $2\pi^0$ from the new tracks, making $3\pi^0$ in total.

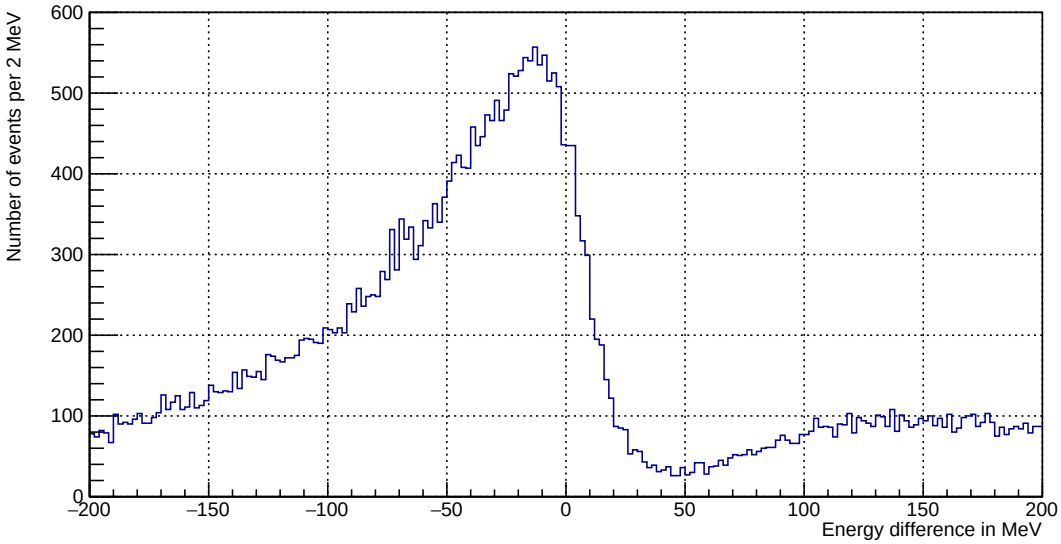

Figure 24: Difference between sum of missing energies and double track energy. A cut is applied at $|(\mathrm{E}_{A2} + \mathrm{E}_{B2}) - \mathrm{E}_2| < 30\mathrm{MeV}$.

6 Analysis

In order to extract the differential cross-section of coherent $3\pi^0$ photoproduction with a forward going deuteron for different beam energies later, only events are selected for which the cosine of polar angle in the centre-of-mass system $\cos(\theta_{\mathrm{CMS}})$ is greater than 0.8°. This results in a solid angle of 0.4π. Furthermore, 3 tagger channels each are combined into one beam energy interval to increase the statistics per interval.

Before the extraction of the differential cross-section, the incoherent background is calculated out first. Then the yield can be determined for each beam energy interval, i.e. the background-corrected absolute number of reconstructed $3\pi^0$d events. This is divided by the flux to obtain the relative number of reconstructed $3\pi^0$d events. By dividing by the detection efficiency, the relative number of produced $3\pi^0$d events is obtained. Finally, this is scaled with the target area density and the solid angle, resulting in the extracted differential cross-section:

$$\left[\frac{\mathrm{d}\sigma}{\mathrm{d}\Omega}\right]_{\mathrm{exp}} = \frac{\text{yield}}{\text{flux} \cdot \text{efficiency} \cdot \text{target area density} \cdot \text{solid angle}} \tag{2}$$

6.1 Incoherent background

Since some protons are misinterpreted as deuterons in the forward spectrometer when distinguishing between coherent and incoherent events, an incoherent background arises in the events that are initially classified as coherent. In order to eliminate the background, the distribution of the missing mass of the reconstructed $3\pi^0$ is plotted for each beam energy interval. A fit function ($\mathrm{f_{fit}}$) is fitted to this distribution, which corresponds to a superposition of a coherent probability density function ($\mathrm{PDF_{coh}}$) with an incoherent probability density function ($\mathrm{PDF_{inc}}$):

$$\mathrm{f_{fit}} = \mathrm{c_{coh}} \cdot \mathrm{PDF_{coh}} + \mathrm{c_{inc}} \cdot \mathrm{PDF_{inc}} \qquad \text{with} \quad \mathrm{c_{coh}}, \mathrm{c_{inc}} \in \mathbb{R} \tag{3}$$

The simulated $2\pi^0$ data are used to determine the coherent PDF. For this purpose, the distribution of the $3\pi^0$ missing mass in simulated events is also plotted for each beam energy interval, which can be seen in Figure 25 for a few selected intervals (black crosses). In all intervals, the peak agrees well with the deuteron mass, as expected, independent of the beam energy. To create the $\mathrm{PDF_{coh}}$ (blue line) for each interval, the distribution is normalised to 1.

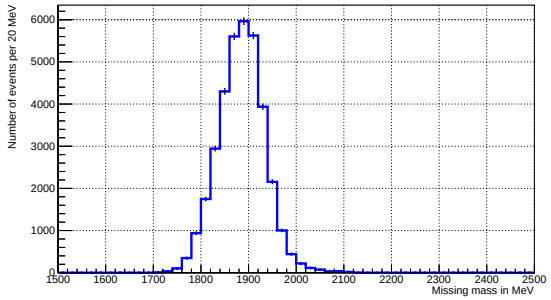

(a) from 759 MeV to 867 MeV

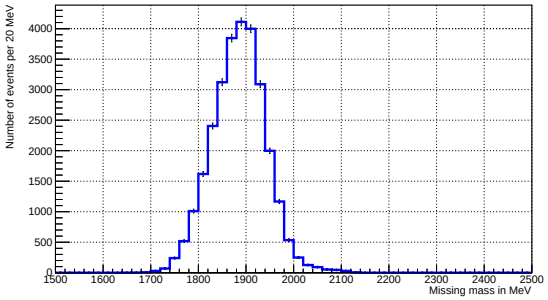

(b) from 867 MeV to 963 MeV

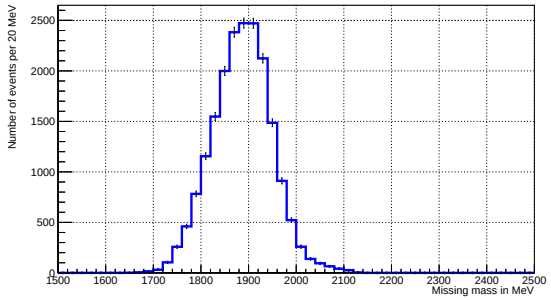

(c) from 963 MeV to 1036 MeV

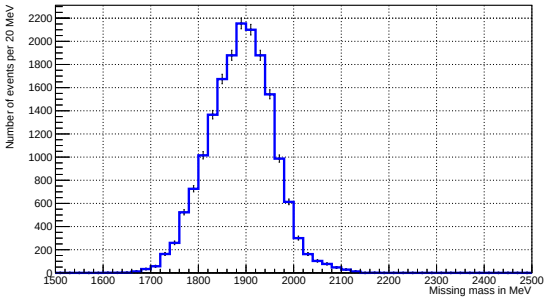

(d) from 1036 MeV to 1109 MeV

Figure 25: Distribution of the $3\pi^0$ missing mass for selected beam energy intervals with simulated coherent data. The blue line is the PDF (not normalised in figure).

To determine the incoherent PDF, real data that have been classified as incoherent, with a proton in the forward spectrometer, are used, since the coherent background can be neglected there. Again, the distribution of the $3\pi^0$ missing mass is plotted for the same intervals as before, which can be seen in Figure 26 (black crosses). In contrast to the simulated coherent events, these distributions are all shifted to the right. The greater the beam energy, the greater the rightward shift. This is also to be expected, since larger beam energies can also cause larger momenta between the proton and the neutron, which result in a higher missing mass. To create the $\mathrm{PDF}_{\mathrm{inc}}$ (blue line) for each interval, the distribution is normalised to 1 again.

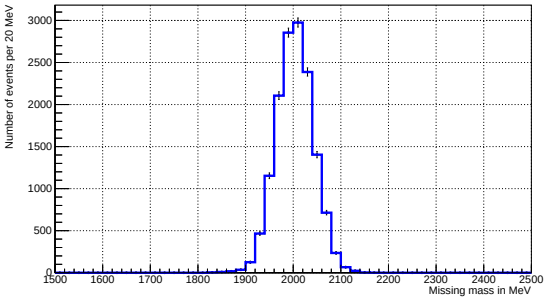

(a) from 759 MeV to 867 MeV

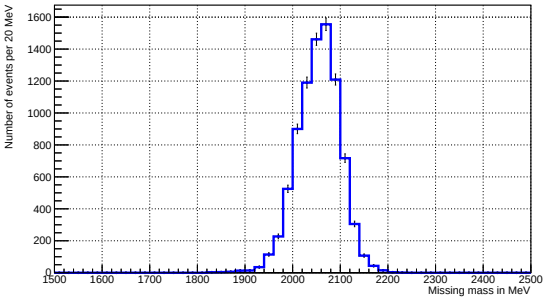

(b) from 867 MeV to 963 MeV

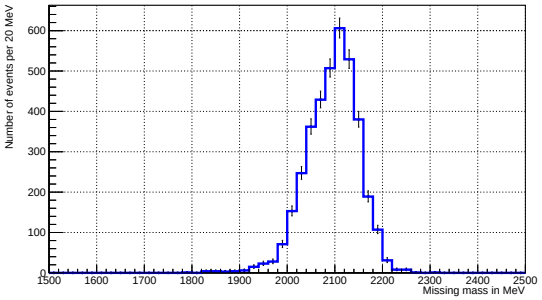

(c) from 963 MeV to 1036 MeV

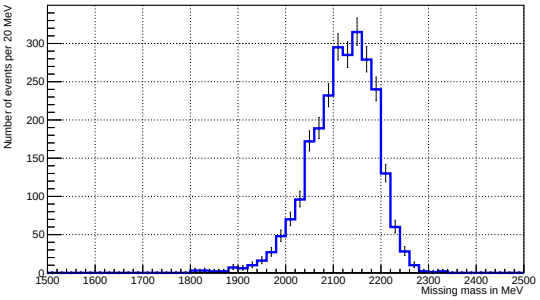

(d) from 1036 MeV to 1109 MeV

Figure 26: Distribution of the $3\pi^0$ missing mass for selected beam energy intervals with real incoherent data. The blue line is the PDF (not normalised in figure).

Finally, the same procedure is followed with the real coherent data. The distributions of the $3\pi^0$ missing masses for the same intervals as before are shown in Figure 27 (black crosses). The fit function (blue line) is then fitted to this, which corresponds to a superposition of the coherent PDF (red line) and the incoherent PDF (green line). The background $c_{inc} \cdot PDF_{inc}$ can then be subtracted from the distribution.

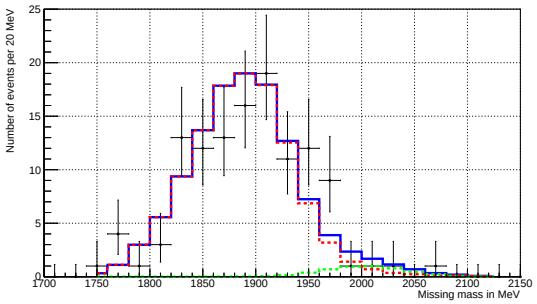

(a) from 759 MeV to 867 MeV

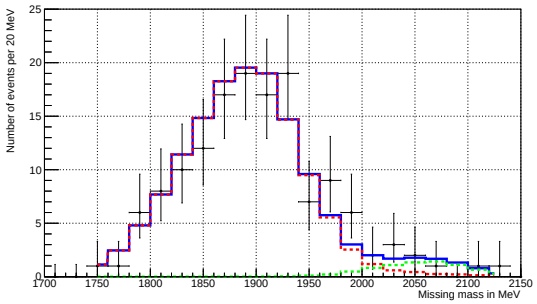

(b) from 867 MeV to 963 MeV

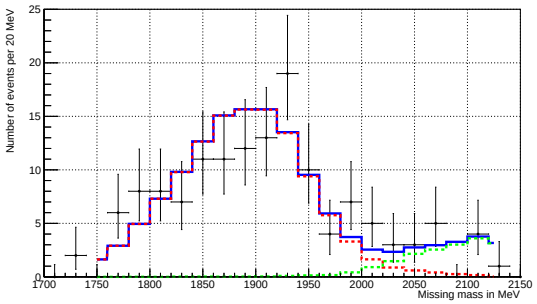

(c) from 963 MeV to 1036 MeV

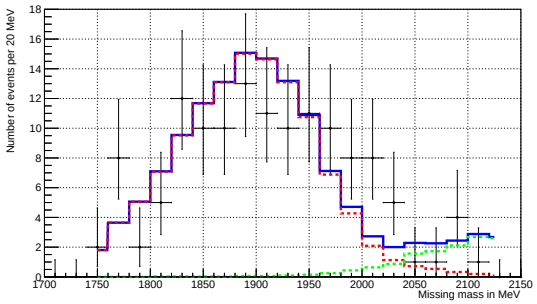

(d) from 1036 MeV to 1109 MeV

Figure 27: Distribution of the $3\pi^0$ missing mass for selected beam energy intervals. The black crosses are real events. Red is the coherent PDF, green the incoherent PDF and blue the superposition of both, i.e. the fit function.

6.2 Yield

The yield then corresponds to the background-corrected distribution integrated over the entire $3\pi^0$ missing mass distribution and thus to the factor c_{coh} in equation 3. For each beam energy interval, the yield is plotted in Figure 28 including the statistical errors. It is also shown in Table 1. The mean energy in each beam energy interval is taken for the beam energy in the plot.

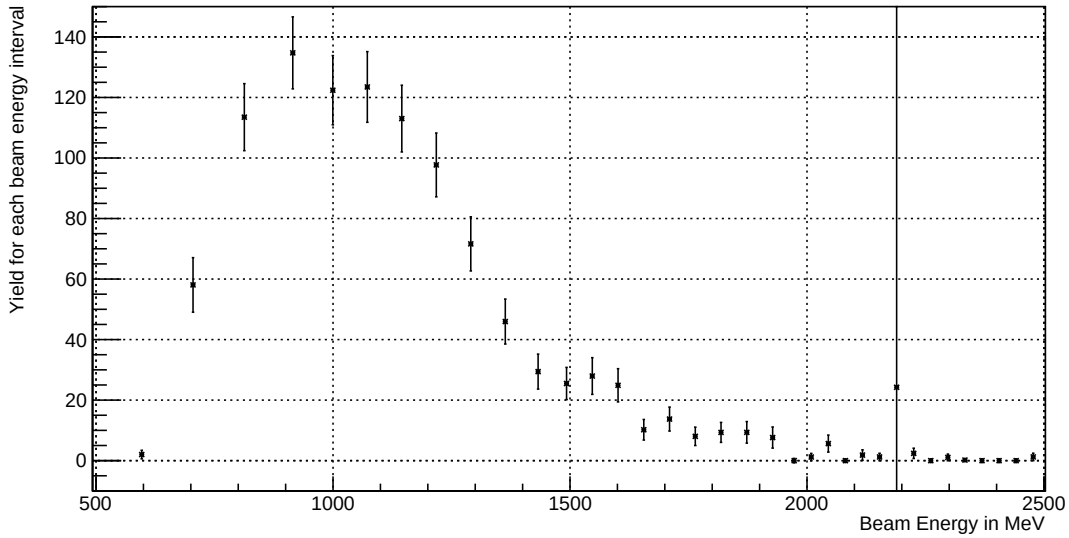

Figure 28: Background-corrected yield per each beam energy interval in coherent $3\pi^0$ photoproduction with forward going deuterons with $\cos(\theta_{\mathrm{CMS}}) > 0.8$.

Beam energy interval	Beam energy in MeV from	to	Background corrected yield	Beam energy interval	Beam energy in MeV from	to	Background corrected yield
0	542	651	2.0 ± 1.4	19	1900	1955	7.6 ± 3.5
1	651	759	58.1 ± 9.0	20	1955	1991	0.0 ± 0.7
2	759	867	113.5 ± 11.1	21	1991	2027	1.2 ± 1.2
3	867	963	134.7 ± 11.9	22	2027	2063	5.6 ± 2.8
4	963	1036	122.4 ± 11.4	23	2063	2099	0.0 ± 0.6
5	1036	1109	123.5 ± 11.7	24	2099	2135	1.8 ± 1.7
6	1109	1181	113.0 ± 11.0	25	2135	2171	1.2 ± 1.2
7	1181	1254	97.7 ± 10.5	26	2171	2207	24.2 ± 807.1
8	1254	1327	71.6 ± 8.9	27	2207	2243	2.4 ± 1.7
9	1327	1400	46.0 ± 7.4	28	2243	2279	0.0 ± 0.6
10	1400	1466	29.4 ± 5.8	29	2279	2315	1.1 ± 1.1
11	1466	1520	25.5 ± 5.3	30	2315	2351	0.2 ± 0.3
12	1520	1574	28.0 ± 6.1	31	2351	2387	0.0 ± 0.6
13	1574	1628	24.9 ± 5.5	32	2387	2423	0.0 ± 0.6
14	1628	1683	10.2 ± 3.4	33	2423	2459	0.0 ± 0.6
15	1683	1737	13.7 ± 4.0	34	2459	2495	1.2 ± 1.2
16	1737	1791	8.0 ± 3.0	35	2496	2531	0.0 ± 0.6
17	1791	1846	9.3 ± 3.3	36	2531	2567	0.3 ± 0.8
18	1846	1900	9.3 ± 3.6	37	2567	2614	0.0 ± 870.5

Table 1: Background-corrected yield for each beam energy interval in coherent $3\pi^0$ photoproduction with forward going deuterons with $\cos(\theta_{\mathrm{CMS}}) > 0.8$.

6.3 Photon flux

The yield corresponds only to the absolute number of reconstructed $3\pi^0$ events per beam energy interval. This alone is not very meaningful because there is not the same photon flux in the different beam energy intervals and the intervals do not have all the same width. To obtain the relative number of reconstructed $3\pi^0$ events, the yield is divided by the flux shown in Figure 29. Here the flux is higher at lower beam energies and decreases as the beam energy increases, which is also to be expected due to the distribution of bremsstrahlung (see also 5.1.1.).

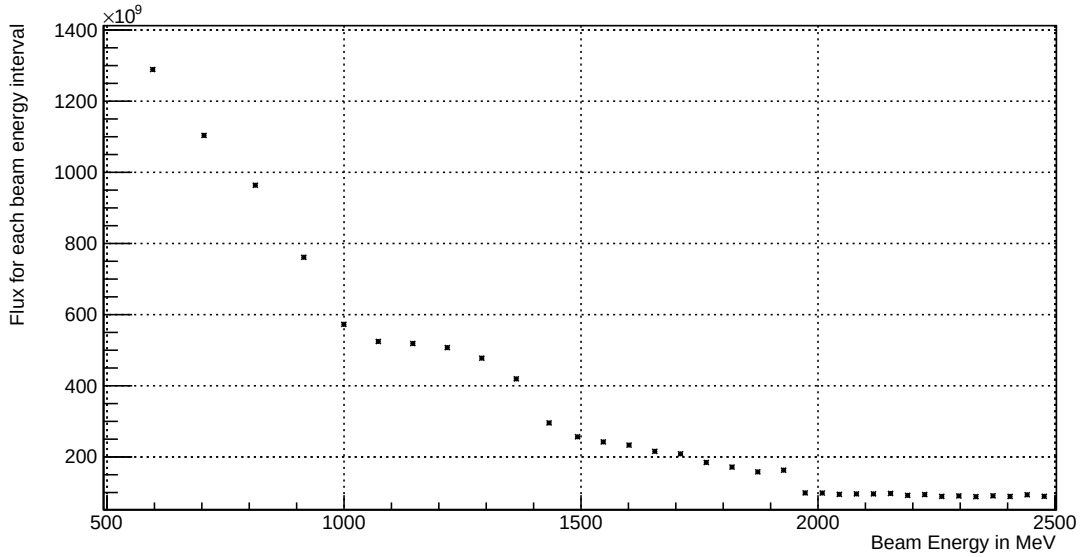

Figure 29: Photon flux in each beam energy interval.

6.4 Detection efficiency

Since only the number of reconstructed $3\pi^0$ events is known so far, but not the number of $3\pi^0$ events that actually took place, the former is divided by the detection efficiency, and thus the probability that an actually occurred $3\pi^0$ event is also reconstructed. To determine the detection efficiency per beam energy interval, the number of reconstructed $3\pi^0$ events in the simulated data is divided by the total number of generated $3\pi^0$ events, separately for each interval. The detection efficiency is shown in Figure 30 and in Table 2 for each beam energy interval. The efficiency initially rises sharply from 2.2 % at around 600 MeV, reaches a plateau of 5.5 % between 800 and 1000 MeV, and then slowly drops to 3 % at 2300 MeV. For higher beam energies above 2315 MeV, the efficiency could not be determined, as probably no generated events occur here. The statistical errors of the efficiencies can be reduced to almost 0 with a sufficiently large amount of simulated data and can thus be neglected compared to the statistical errors of the background-corrected yield.

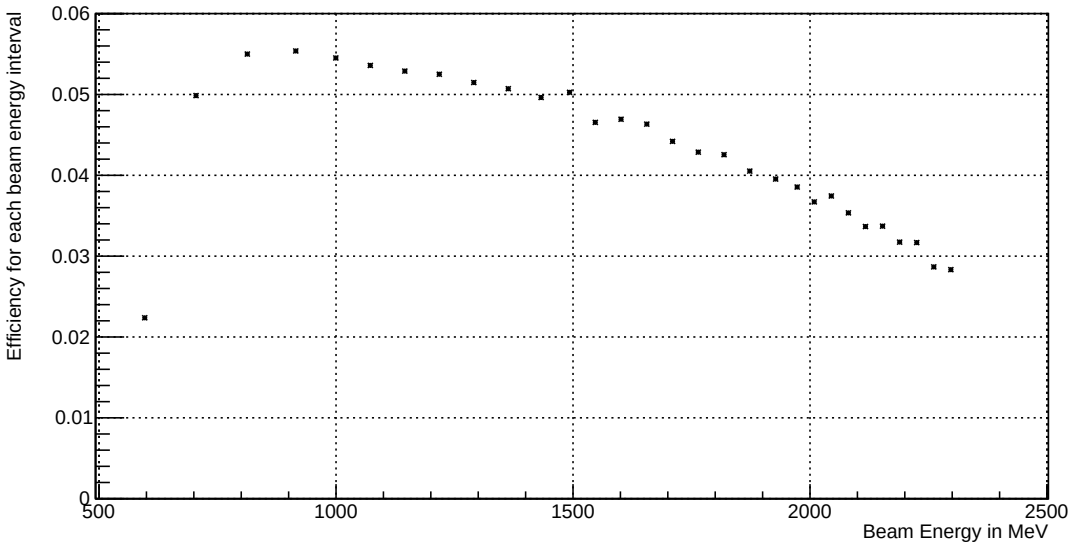

Figure 30: Efficiency in each beam energy interval in coherent $3\pi^0$ photoproduction with forward going deuterons with $\cos(\theta_{\mathrm{CMS}}) > 0.8$.

Beam energy interval	**Beam energy in MeV**		**Detection efficiency in %**	**Beam energy interval**	**Beam energy in MeV**		**Detection efficiency in %**
	from	**to**			**from**	**to**	
0	542	651	2.24	19	1900	1955	3.95
1	651	759	4.99	20	1955	1991	3.86
2	759	867	5.50	21	1991	2027	3.67
3	867	963	5.54	22	2027	2063	3.74
4	963	1036	5.45	23	2063	2099	3.54
5	1036	1109	5.36	24	2099	2135	3.37
6	1109	1181	5.29	25	2135	2171	3.37
7	1181	1254	5.25	26	2171	2207	3.17
8	1254	1327	5.15	27	2207	2243	3.17
9	1327	1400	5.07	28	2243	2279	2.87
10	1400	1466	4.96	29	2279	2315	2.83
11	1466	1520	5.03	30	2315	2351	N/A
12	1520	1574	4.65	31	2351	2387	N/A
13	1574	1628	4.69	32	2387	2423	N/A
14	1628	1683	4.63	33	2423	2459	N/A
15	1683	1737	4.42	34	2459	2495	N/A
16	1737	1791	4.29	35	2496	2531	N/A
17	1791	1846	4.26	36	2531	2567	N/A
18	1846	1900	4.05	37	2567	2614	N/A

Table 2: Detection efficiency for each beam energy interval in coherent $3\pi^0$ photoproduction with forward going deuterons with $\cos(\theta_{\mathrm{CMS}}) > 0.8$.

7 Results

7.1 Differential cross-section

The differential cross-section $\left[\frac{d\sigma}{d\Omega}\right]_{exp}$ for forward going deuterons with $\cos(\theta_{CMS}) > 0.8$ can then be extracted with equation 2. The results are shown in Figure 31 and in Table 3. The $\left[\frac{d\sigma}{d\Omega}\right]_{exp}$ can not be determined for energies above 2315 MeV, since the efficiency can not be determined here either. The maximum occurs in the beam energy interval between 1036 MeV and 1109 MeV (corresponding centre-of-mass energy between 2720 MeV and 2770 MeV) with (7.4 ± 0.7)nb/sr, but no resonance-like structures can be seen.

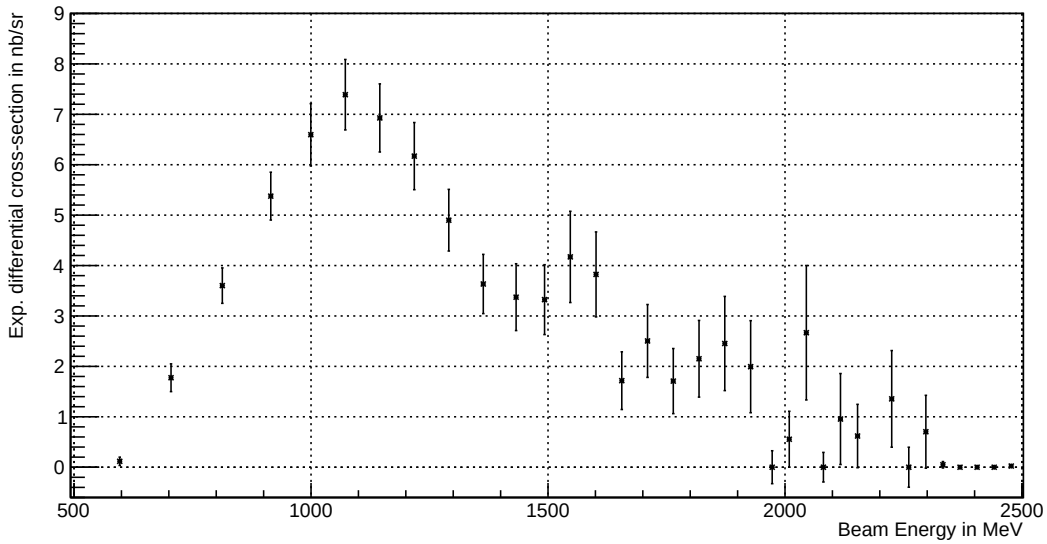

Figure 31: Extracted differential cross-section in different beam energy intervals in coherent $3\pi^0$ photoproduction with forward going deuterons with $\cos(\theta_{CMS}) > 0.8$.

Beam energy interval	Beam energy in MeV from	to	Differential cross-section in nb/sr	Beam energy interval	Beam energy in MeV from	to	Differential cross-section in nb/sr
0	542	651	0.1 ± 0.1	19	1900	1955	2.0 ± 0.9
1	651	759	1.8 ± 0.3	20	1955	1991	0.0 ± 0.3
2	759	867	3.6 ± 0.4	21	1991	2027	0.6 ± 0.6
3	867	963	5.4 ± 0.5	22	2027	2063	2.7 ± 1.3
4	963	1036	6.6 ± 0.6	23	2063	2099	0.0 ± 0.3
5	1036	1109	7.4 ± 0.7	24	2099	2135	1.0 ± 0.9
6	1109	1181	6.9 ± 0.7	25	2135	2171	0.6 ± 0.6
7	1181	1254	6.2 ± 0.7	26	2171	2207	14.0 ± 465.0
8	1254	1327	4.9 ± 0.6	27	2207	2243	1.4 ± 1.0
9	1327	1400	3.6 ± 0.6	28	2243	2279	2.8 ± 0.4
10	1400	1466	3.4 ± 0.7	29	2279	2315	0.7 ± 0.7
11	1466	1520	3.3 ± 0.7	30	2315	2351	N/A
12	1520	1574	4.2 ± 0.9	31	2351	2387	N/A
13	1574	1628	3.8 ± 0.8	32	2387	2423	N/A
14	1628	1683	1.7 ± 0.6	33	2423	2459	N/A
15	1683	1737	2.5 ± 0.7	34	2459	2495	N/A
16	1737	1791	1.7 ± 0.6	35	2496	2531	N/A
17	1791	1846	2.2 ± 0.8	36	2531	2567	N/A
18	1846	1900	2.5 ± 0.9	37	2567	2614	N/A

Table 3: Extracted differential cross-section for each beam energy interval in coherent $3\pi^0$ photoproduction with forward going deuterons with $\cos(\theta_{\mathrm{CMS}}) > 0.8$.

7.2 Comparison to coherent $2\pi^0$ photoproduction

For a comparison, the same analysis is done for coherent $2\pi^0$ photoproduction. The results can be seen in Figure 32 and in Table 4. At energies above 1991 MeV, the value is orders of magnitude smaller than the error, so that no differential cross-section statistically significantly different from 0 can be extracted. The maximum occurs in the beam energy interval between 867 MeV and 963 MeV (corresponding centre-of-mass energy between 2601 MeV and 2669 MeV) with (6.2 ± 0.5)nb/sr. The centre-of-mass energy of the maximum lies in the range of the isoscalar dibaryon resonance with a mass of 2.63 GeV, which was found in Ref. [4]. But this can also be a random coincidence and does not necessarily indicate a resonance.

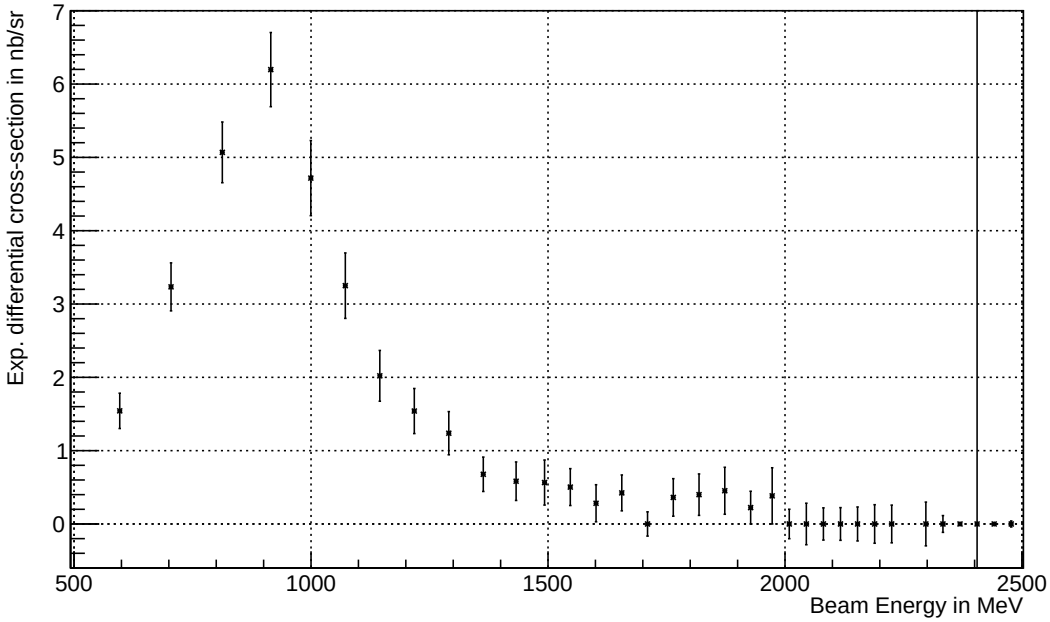

Figure 32: Extracted differential cross-section in different beam energy intervals in coherent $2\pi^0$ photoproduction for forward going deuterons with $\cos(\theta_{\mathrm{CMS}}) > 0.8$.

Beam energy interval	Beam energy in MeV from	to	Differential cross-section in nb/sr
0	542	651	1.5 ± 0.2
1	651	759	3.2 ± 0.3
2	759	867	5.1 ± 0.4
3	867	963	6.2 ± 0.5
4	963	1036	4.7 ± 0.5
5	1036	1109	3.3 ± 0.4
6	1109	1181	2.0 ± 0.3
7	1181	1254	1.5 ± 0.3
8	1254	1327	1.2 ± 0.3
9	1327	1400	0.7 ± 0.2
10	1400	1466	0.6 ± 0.3
11	1466	1520	0.6 ± 0.3
12	1520	1574	0.5 ± 0.3
13	1574	1628	0.3 ± 0.3
14	1628	1683	0.4 ± 0.2
15	1683	1737	0.0 ± 0.2
16	1737	1791	0.4 ± 0.2
17	1791	1846	0.4 ± 0.3
18	1846	1900	0.5 ± 0.3
19	1900	1955	0.2 ± 0.2
20	1955	1991	0.4 ± 0.4

Table 4: Extracted differential cross-section for each beam energy interval in coherent $2\pi^0$ photoproduction with forward going deuterons with $\cos(\theta_{\mathrm{CMS}}) > 0.8$.

7.3 Invariant mass of $2\pi^0$d and π^0d

Finally, a look into the invariant mass distributions of $2\pi^0$d and π^0d is taken with a beam energy between 939 MeV and 1303 MeV. Figure 33 shows the invariant mass distribution of $2\pi^0$d in simulated and real data. The maxima of both distributions lie between 2400 MeV and 2500 MeV. The distribution of the real events is quite similar to the simulated distribution and a resonance-like structure is thus not observed. The invariant mass of π^0d shown in Figure 34 has a maximum of around 2150 MeV. Here, too, no resonance can be seen at first view, even though the maximum appears in the same region as the isovector 2.14 GeV dibaryon from Ref. [4]. However, this is not surprising as it is just above the threshold for the production of π^0d.

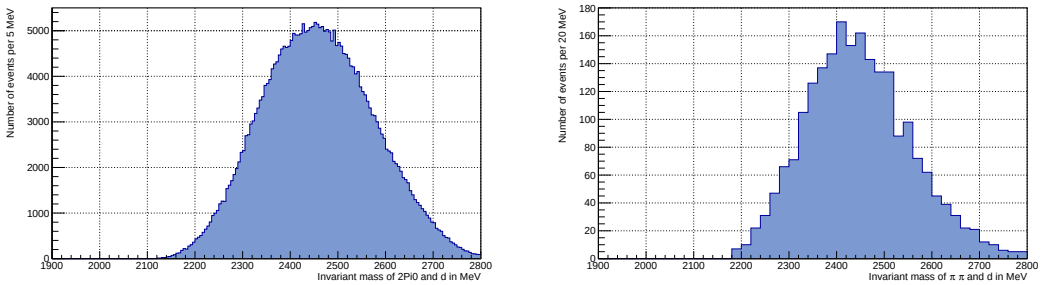

(a) Simulated data (b) Real data

Figure 33: Invariant mass of $2\pi^0$d in $3\pi^0$ photoproduction.

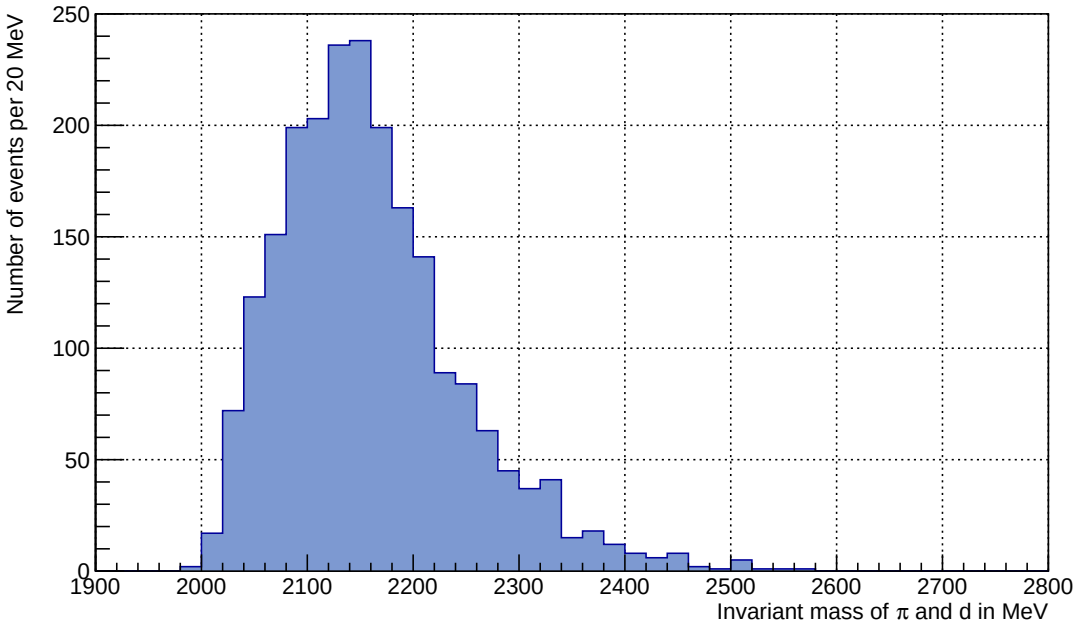

Figure 34: Invariant mass of π^0d in $3\pi^0$ photoproduction (real data).

8 Summary

The differential cross-section $\left[\frac{d\sigma}{d\Omega}\right]_{exp}$ of coherent $3\pi^0$ photoproduction off a deuteron with forward going deuterons ($\cos(\theta_{CMS}) > 0.8$) was extracted for beam energies between 542 MeV and 2614 MeV. A maximum in the differential cross-section lies at a centre-of-mass energy between 2720 MeV and 2770 MeV, which corresponds to a beam energy range between 1036 MeV and 1109 MeV, so it is shifted to a higher energy compared to the maximum in coherent $2\pi^0$ photoproduction. However, with (7.4 ± 0.7)nb/sr it has a similar strength within the errors as the maximum in coherent $2\pi^0$ photoproduction. Furthermore, the invariant mass distributions of $2\pi^0$d and π^0d were scanned for obvious resonance-like structures.

Based on the results of previous experiments where dibaryon resonances have been found, as well as theoretical predictions, one could expect isovector resonances in the differential cross-section of $\gamma d \to 3\pi^0 d$ and the invariant mass of π^0d as well as isoscalar resonances in the invariant mass of $2\pi^0$d. However, no indication of resonance-like structures was seen in this exploratory study of coherent $3\pi^0$ photoproduction off a deuteron. Further research is therefore needed in this reaction channel.

List of figures

List of tables

List of references

[1] Forschungszentrum Jülich. *Exotic Particle Confirmed.* (2014). URL: https://www.fz-juelich.de/SharedDocs/Pressemitteilungen/UK/EN/2014/14-05-23exotisches-teilchen.html. (accessed: 26/09/2021).

[2] P. Adlarson et al. "Evidence for a New Resonance from Polarized Neutron-Proton Scattering". In: *Phys. Rev. Lett.* 112.20 (2014), p. 202301. DOI: 10.1103/PhysRevLett.112.202301. arXiv: 1402.6844 [nucl-ex].

[3] Man Ho Chan. "The Decaying and Scattering Properties of the d*(2380) Hexaquark Bose-Einstein Condensate Dark Matter". In: *The Astrophysical Journal* 898.2 (2020), p. 132. DOI: 10.3847/1538-4357/ab9df6. URL: https://doi.org/10.3847/1538-4357/ab9df6.

[4] T. Ishikawa et al. "Non-strange dibaryons studied in coherent double neutral-meson photoproduction on the deuteron". In: *EPJ Web Conf.* 241 (2020). Ed. by R. Beck et al., p. 01007. DOI: 10.1051/epjconf/202024101007.

[5] M. Gell-Mann. "The Eightfold Way: A Theory of strong interaction symmetry". In: (Mar. 1961). DOI: 10.2172/4008239.

[6] J. Rosner. "The Eightfold Way". In: (Oct. 2001).

[7] M. Gell-Mann. "A schematic model of baryons and mesons". In: *Physics Letters* 8.3 (1964), pp. 214–215. ISSN: 0031-9163. DOI: https://doi.org/10.1016/S0031-9163(64)92001-3. URL: https://www.sciencedirect.com/science/article/pii/S0031916364920013.

[8] P.A. Zyla et al. "Review of Particle Physics". In: *PTEP* 2020.8 (2020), p. 083C01. DOI: 10.1093/ptep/ptaa104.

[9] F. J. Dyson and N. Xuong. "$Y = 2$ States in Su(6) Theory". In: *Phys. Rev. Lett.* 13 (26 1964), pp. 815–817. DOI: 10.1103/PhysRevLett.13.815. URL: https://link.aps.org/doi/10.1103/PhysRevLett.13.815.

[10] P. Adlarson et al. "Abashian-Booth-Crowe Effect in Basic Double-Pionic Fusion: A New Resonance?" In: *Physical Review Letters* 106.24 (2011). ISSN: 1079-7114. DOI: 10.1103/physrevlett.106.242302. URL: http://dx.doi.org/10.1103/PhysRevLett.106.242302.

[11] T. Ishikawa et al. "First measurement of coherent double neutral-pion photoproduction on the deuteron at incident energies below 0.9 GeV". In: *Phys. Lett. B* 772 (2017), pp. 398–402. DOI: 10.1016/j.physletb.2017.04.010. arXiv: 1610.05532 [nucl-ex].

[12] T. Ishikawa et al. "Non-strange dibaryons studied in the $\gamma d \to \pi^0\pi^0 d$ reaction". In: *Phys. Lett. B* 789 (2019), pp. 413–418. DOI: 10.1016/j.physletb.2018.12.050. arXiv: 1805.08928 [nucl-ex].

[13] Alef, S., Bauer, P., Bayadilov, D. et al. "The BGOOD experimental setup at ELSA." In: *Eur. Phys. J. A* 56 (2020), p. 104. URL: https://doi.org/10.1140/epja/s10050-020-00107-x.

[14] W. Hillert, A. Balling, O. Boldt et al. *Beam and spin dynamics in the fast ramping storage ring ELSA: Concepts and measures to increase beam energy, current and polarization.* 2017. URL: https://doi.org/10.1051/epjconf/201713405002.

[15] Ianik Plante and Francis Cucinotta. "Cross sections for the interactions of 1eV-100MeV electrons in liquid water and application to Monte-Carlo simulation of HZE radiation tracks". In: *New Journal of Physics* 11 (June 2009), p. 063047. DOI: 10.1088/1367-2630/11/6/063047.

[16] Bureau International des Poids et Mesures. *The International System of Units (SI).* 2019. URL: https://www.bipm.org/en/measurement-units. (accessed: 26/09/2021).

I hereby declare that the work presented here was formulated by myself and that no sources or tools other than those cited were used.

Bonn, 30th September 2021 A. Stirner

date signature